JOURNAL OF GEOPHYSICAL RESEARCH, VOL. 102, NO. B3, PAGES 5423-5453, MARCH 10, 1997

Three-dimensional V_P and V_P/V_S Velocity Models of the Los Angeles basin and central Transverse Ranges, California

Egill Hauksson and Jennifer S. Haase

Seismological Laboratory, Division of Geological and Planetary Sciences
California Institute of Technology, Pasadena

Abstract. We use P and S arrival times from 5225 earthquakes and 53 explosions, recorded by the Southern California Seismographic Network, to invert for the three-dimensional P- velocity (V_P) and the P and S-velocity ratio (V_P/V_S) in the central Transverse Ranges and the Los Angeles basin. To model long-wavelength features of the velocity structure, we invert for the models by interpolating models determined successively from a sparse, medium, to a dense grid, with 40, 20, and 10 km spacing of horizontal grid nodes. Layers of grid nodes are placed at depths of 1, 4, 6, 8, 12, 16, and 20 km. The data variance decreased about 80% in the gradational inversion. Ample data from the 1994 Northridge and other earthquake sequences, the rich background seismicity, and the dense station distribution along with controlled sources made the model well resolved, except along the edges, to the southwest in the offshore region, and at depths greater than 20 km. The V_P model images the shape of the Los Angeles and east Ventura basins down to depths of 8 and 12 km. Three low-velocity areas at 1 km depth in the Los Angeles basin that coincide with recent sediment depositional areas are also imaged. The north edge of the Peninsular Ranges, the Santa Monica, and the San Gabriel Mountains, form discontinuous high-velocity ridges extending to depths of 20 km. The high V_P/V_S ratios in the near surface are consistent with high pore fluid pressures in the basin sediments. At depth beneath the east Ventura basin the high V_P/V_S and high V_P suggest the presence of ophiolitic assemblages or mid-Miocene volcanics. In contrast, a body with normal V_P and low V_P/V_S that is identified in the upper crust beneath Santa Monica Bay may be a fragment of quartz-rich continental crust. The V_P model of both the Ventura and the Los Angeles basins shows features that suggest deformation of the hanging wall or basin closure. At seismogenic depths of 16 km the hypocenters of moderate-sized and large earthquakes are located within or adjacent to high-V_P-velocity bodies. In most cases these high-velocity bodies form the upper block, consistent with shortening of the lower crust as described in thick-skinned tectonic interpretations.

Introduction

We have used P and S arrival time data from regional earthquakes and shots to determine three-dimensional (3-D) V_P and V_P/V_S models for the central Transverse Ranges and the Los Angeles basin (Figure 1). Such 3-D V_P and V_P/V_S models are needed to improve our understanding of geological structures and the complex regional tectonics [*Hauksson*, 1990]. In particular, the obvious presence of major deep basins juxtaposed against large mountain ranges implies the existence of strong lateral variations in the velocity structure.

Although a significant body of knowledge about the geology and tectonics of the Los Angles region is available, our understanding of the basement rocks beneath the major basins and the geological structures beneath the mountain ranges is limited. For instance, the detailed near-surface shapes of the east Ventura and Los Angeles basins have been mapped using geological data and at greater depths from gravity data and borehole data [e.g., *Yerkes et al.*, 1965; *Wright*, 1991; *Yeats et al.*, 1994]. On the other hand, the detailed configuration of laminated structures within the San Gabriel Mountains is not well understood [e.g., Silver, 1995]. This study contributes to our knowledge of the regional tectonics by providing detailed velocity structure within as well as beneath the basins and the major mountain ranges such as San Gabriel, Santa Monica Mountains, and north end of the Peninsular Ranges. In addition, we hope to identify structural features such as deformation of the hanging wall related to reverse faults at the base of the mountain ranges and concealed faults beneath the basin sediments that form potential source regions for major earthquakes. In particular, the detailed velocity structure of the aftershock zone of the 1994 Northridge earthquake that occurred on a concealed fault along the south side of the east Ventura basin

Paper number 96JB03219.
0148-0227/97/96JB-03219$09.00

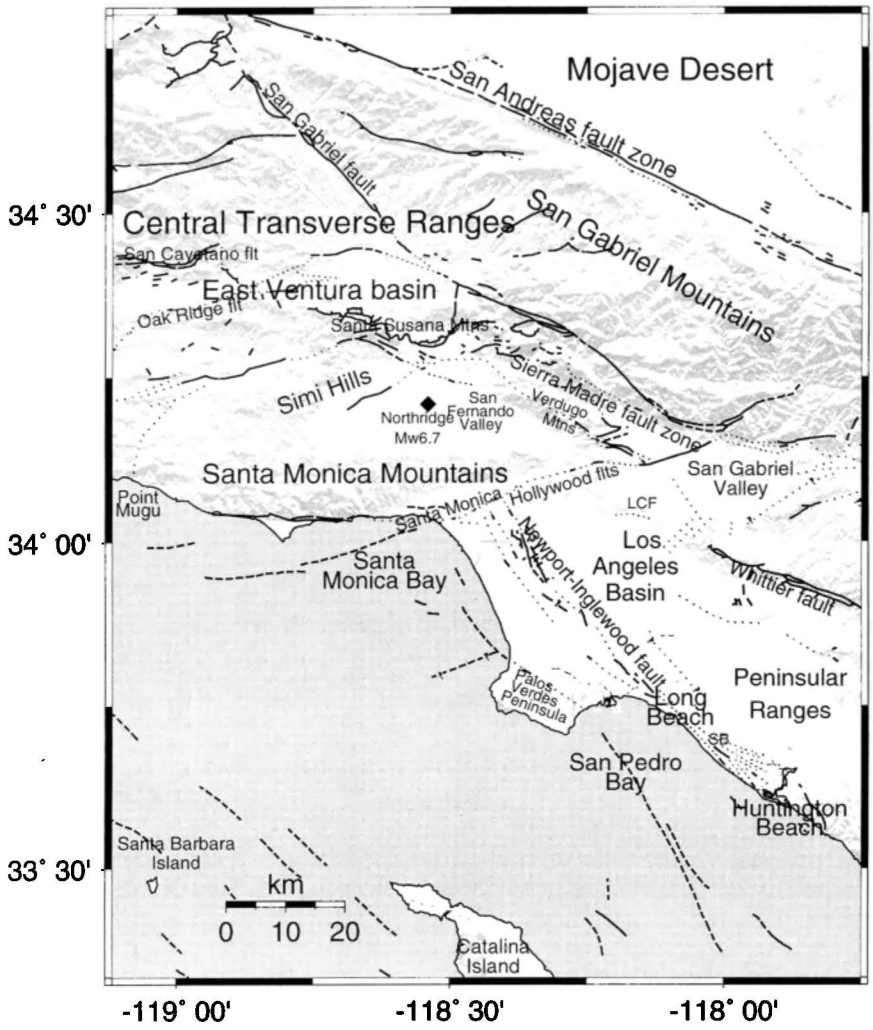

Figure 1. Map of study area showing the central Transverse Ranges and the Los Angeles basin in southern California. The solid diamond is the epicenter of the 1994 Northridge earthquake. Major faults from *Jennings* [1975] are shown, solid where exposed and dashed or dotted where inferred. LCF, Las Cienegas fault; SB, Sunset Beach. This and other maps and cross sections are done using Generic Mapping Tools software [*Wessel and Smith*, 1991].

[*Hauksson et al.*, 1995] can be imaged by the abundant aftershock arrival time data. Such an image can be compared with available geological models by *Davis and Namson* [1994] and *Yeats and Huftile* [1995].

The 3-D models presented here can also be used to model path and site effects for strong ground motions from earthquakes located beneath the Los Angeles basin as well as for events occurring farther away along the San Andreas fault [*e.g., Olsen et al.*, 1995]. Such path and site effects can either amplify or attenuate strong ground motion causing complex patterns of shaking at the surface. For instance, *Haase et al.* [1996] showed that the long duration of the ground motions of the 1994 Northridge earthquake recorded in the Los Angeles basin could in part be explained by the 3-D velocity structure of the region.

We use the SIMULPS inversion technique developed by *Thurber* [1983; 1993] to determine models based first on a coarse grid that in turn is averaged to a denser grid and the inversion is run again; here this approach is referred to as a gradational inversion, used extensively by *Eberhart-Phillips* [1990]. We use the gradational inversion approach because the emphasis of this work is to determine realistic 3-D models with velocity variations that in some cases may exceed 50% over short distances. This differs from most tomographic studies that emphasize the sharpness of the image and resolved patterns that are a small fraction (±5 to ±10%) of the true structural variations [e.g., *Aki*, 1993; *Zhao and Kanamori*, 1995]. Furthermore, the models presented in this study are more detailed than, for instance, models derived by *Hearn and Clayton* [1986], *Magistrale et al.* [1992], *Sung and Jackson* [1992], and *Hu et al.* [1994]. Our models also extend over a larger area than previously available V_P tomographic models of the Northridge region [*Mori et al.*, 1995; *Zhao and Kanamori*, 1995]. We use a different slow-starting model to evaluate the influence of the initial model on the final model. As a check of the validity of the model we relocate 53 shots and compare their calculated location with the true location. The details of the modeling and uncertainty analysis are presented in the Appendix where we document how the travel time residuals (in essence, the signals) that are being inverted decrease with progressively smaller grid size. We

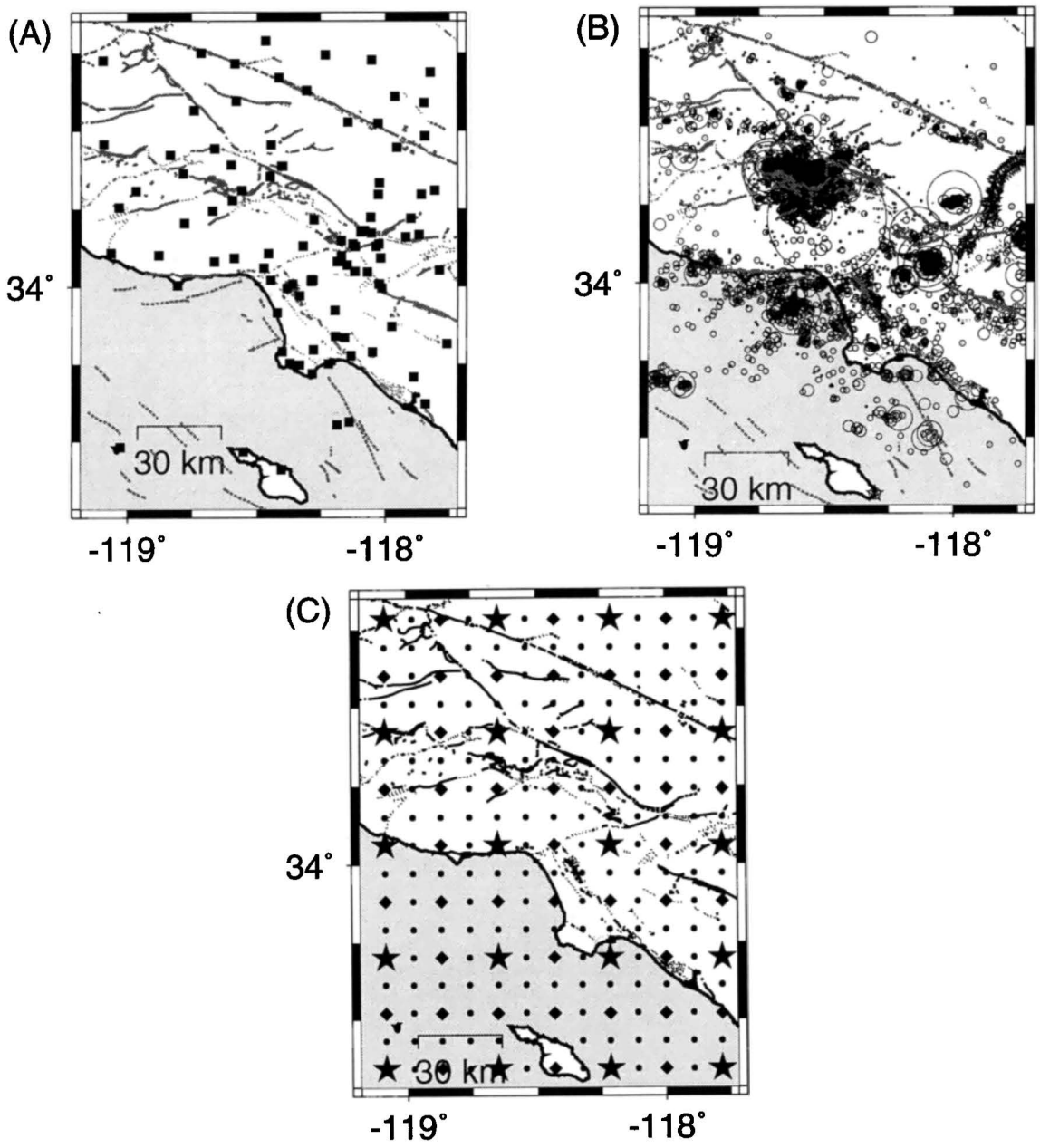

Figure 2. (a) Seismographic stations that recorded the *P* and *S* arrival times. (b) The earthquakes (circles) and shots (stars) used in the inversion (1973-1994). Note shots south of Long Beach and on Catalina Island. (c) The three 3-D velocity grids, 40 km (stars), 20 km (diamonds), and 10 km (solid circles).

calculate the full resolution matrix and the corresponding spread function, to identify well-resolved regions of the model [*Toomey and Foulger,* 1989].

Data and Analysis

We chose the study region to determine the best possible 3-D velocity model for the central Transverse Ranges, including the Northridge aftershock region, and the Los Angeles basin down to depths of 20 km. Only data from stations and earthquakes within the model area were included in this study (Figures 2a and 2b). The island stations on Santa Barbara and Catalina Islands that are located to the south and southwest provided rays traveling deep beneath the model region.

Data Set

The data set used in the inversion consisted of 119,000 *P* arrival times and 16,000 *S* arrival times from 5225 local earthquakes that occurred from 1973 to 1995. The *S* data were included in the form of *S-P* times to constrain the focal depths of the events and to determine the 3-D V_P/V_S model [*Thurber,* 1993]. The included events are located within the model area and provide best available ray coverage of the region. Events of $M \geq 2.0$ with more than 15 phases that occurred from 1973 to 1993 were included. In addition a few events with 10 to 15 phases and located in aseismic parts of the model were included. A total of 2200 Northridge aftershocks with more than 20 phases were also included. Data from these earthquakes were

recorded by the Southern California Seismographic Network (SCSN) operated by the California Institute of Technology (Caltech) and the U.S. Geological Survey, and the Los Angeles Basin Network operated by the University of Southern California. A deployment of portable instruments organized by the Southern California Earthquake Center (SCEC) following the 1994 Northridge earthquake provided additional arrival times for Northridge aftershocks [*Edelman et al.*, 1994]. These data allowed more accurate modeling of the north end of the Los Angeles basin. The availability of the Los Angeles Regional Seismic Experiment (LARSE) [*Fuis et al.*, 1996] shot data recorded by the SCSN improved the resolution of the velocities at shallow depth, especially in the eastern part of the model.

Arrival times at permanent SCSN stations from 49 shots, which were part of the LARSE [*Fuis et al.*, 1996] provided an absolute reference for the 3-D velocity model and constrained velocities at shallow depth. This paper, however, does not include analysis of LARSE field data, which is being done by LARSE investigators [e.g., *Fuis et al*, 1996; *Norris and Clayton*, 1995; *Hafner and Clayton*, 1995; *Lutter et al.*, 1995]. Data from two (1981 and 1995) Catalina Island shots [*Given and Koesterer*, 1983; G. Fuis, written communication, 1995], the 1987 Whittier Narrows shot [*Perkins*, 1988], and a 1984 Azusa quarry shot (E. Hauksson, unpublished data, 1984) were also used (Figure 2b).

Inversion Approach

We have used the inversion technique and computer codes (SIMULPS) developed by *Thurber* [1983; 1993], and *Eberhart-Phillips* [1990], including documentation by *Evans et al.* [1994]. We specify the initial 3-D velocity model as a 3-D grid of points, and velocities are interpolated linearly between the points. The ray tracing is done using an approximate 3-D algorithm with curved non planar ray paths [*Um and Thurber*, 1987]. The damped least squares solution to the linearized problem is given by

$$m = (M^T M + L)^{-1} M^T t$$

where m is a vector of model perturbations, t is a vector of travel time residuals, L is a diagonal matrix of damping parameters, and M is a matrix of partial derivatives constructed according to the parameter separation techniques of *Pavlis and Booker* [1980]. Each inversion for the 3-D velocity model consisted of three model iterations, and each model iteration was followed by up to three iterations of hypocentral relocations using the new model.

We use the gradational inversion approach. This approach consists of (1) starting with a horizontally uniform initial model and inverting for a model (LA1-40) using a coarse 40 km grid; (2) interpolating the 40 km model with a 20 km grid; (3) using the 20 km interpolated model as a starting model and the relocated events to invert for a 20 km grid model (LA1-20); (4) interpolating the 20 km model with a 10 km grid; and (5) using the 10 km interpolated model as a starting model and the relocated events to invert for a final 10 km grid model (LA1-10). The outer edge of nodes was held fixed in the 10 km grid inversion. We stopped at 10 km grid because calculating a denser grid such as a 5 km grid was too time consuming. This gradational approach allows us to capture successively smaller and smaller wavelengths of the velocity structure into the model. This approach also allows for some inaccuracy in the starting model because we invert first for a coarse model using the 40 km grid which in essence provides a refined starting model. To evaluate the effect of the gradational approach, we also compared the gradational inversion model (LA1-10) with a model (LA2-10) determined from a 10 km grid with uniform layer velocities. To test the dependence of the final model on the starting model, we used a slow Los Angeles basin type starting model and repeated the gradational approach determining models, LA3-40, LA3-20, and LA3-10. The LA2-10 and LA3-10 models had significantly higher final data variance than the LA1-10 model (Table 1). The initial and final average models and the standard deviation for each grid layer are listed in Table 2.

To refine hypocenters of earthquakes in the Northridge region, *Hauksson et al.* [1995] used VELEST [*Kissling et al.*, 1994] to determine a one-dimensional (1-D) model for the region. This model is similar to the V_P model of *Hadley and Kanamori* [1977] except for the 1 km deep layer that was added to account for low near-surface velocities in the major basins. This initial model that is used in this study is well fit by the data because the 3-D coarse 40 km grid model (LA1-40) differ in average velocity less than 0.16 km/s for the top two layers and 0.02 km/s for subsequent layers. The slower initial model for model LA3-10 that changed by 0.48 km/s in the top layers and from 0.1 to 0.4 km/s in the deeper layers also had a higher final data variance (Table 1).

The grid area extended 120 km in the east-west direction and 160 km in the north-south direction (Figure 2c). The depth spacing remained constant in all the inversions with grid layers at 1, 4, 6, 8, 12, 16, and 20 km depth. To avoid Moho complications, a distance cut off at 120 km with a linear taper to zero at 140 km distance was applied because *Magistrale et al.* [1992] showed that in southern California *Pn* phases only need to be taken into account for epicentral distances greater than 150 km. A residual filter of 1.0 s, 1.75 s, and 2.75 s with linear taper from one to zero was applied to remove high residual data.

Because we expected extreme variations in velocity structure in the region, we used different inversion parameters than were used in other studies [e.g., *Eberhart-Phillips and Michael*, 1993]. We did not use the maximum permissible velocity perturbation that is often restricted to a small value. We only the damping stabilized the inversion. We kept the initial damping high for the 40 and 20 km grids (5000 for V_P and 200 for V_P/V_S, see Appendix). We did not allow station delays because all the stations are located within the model region. The values of 5000 and 200 were chosen by plotting data variance versus model length (defined here as the model standard deviation) and choosing a value that provided a reasonable trade-off between reduction in data variance and model length.

We discuss the damping for the final 10 km grid 3-D

Table 1. Data Variance for the Three-Dimensional Velocity Models

Model	Grid, km	*P* Damping	*S-P* Damping	Iterations	Data Variance Initial, s^2	Data Variance Final, s^2	Model Variance *P*, $(km/s)^2$	Model Variance *S-P*, $(km/s)^2$	Remarks
LA1-40	40	5000	200	3	0.08890	0.05221	0.07601	0.00166	ave. starting model
LA1-20	20	5000	200	3	0.05258	0.03595	0.07666	0.01286	
LA1-10	10	150	15	3	0.03645	0.02055	0.12679	0.02341	preferred model
LA2-10	10	1500	200	5	0.09060	0.02986	0.04659	0.00042	uniform starting model
LA3-40	40	5000	200	3	0.12094	0.05504	0.12676	0.00140	slow starting model
LA3-20	20	5000	200	3	0.05515	0.03610	0.108876	0.00115	
LA3-10	10	150	15	3	0.03658	0.02445	0.107558	0.00251	

model in the Appendix. Initial test runs showed that if the damping was too high, the model did not change significantly. Conversely, if the damping value was too low, parts of the top two layers of the model would quickly gain unreasonably high velocities in the San Gabriel Mountains. In addition, isolated grid points in the Los Angeles basin tend to gain very low values while other points with less dense ray coverage did not change significantly. To test for some of the effects of parameterization, several different vertical grid layers were tried and the horizontal grid was repositioned within the model area. All of these attempts produced similar models as LA1-10, confirming that LA1-10 is a representative model of the region.

To evaluate the effects of uneven ray coverage, station distribution, and data errors on the model, the full resolution matrix was determined. As discussed in the Appendix, we use the spread function of each averaging vector rather than the diagonal elements of the resolution matrix to evaluate how well the model parameters are resolved [*Toomey and Foulger,* 1989]. In a dense grid model, each grid node may have low values of the diagonal elements of the resolution matrix while the spread function values may also be low, indicating adequate resolution. The smaller the value of the spread function, the more compact the averaging vector and the better the volume averaging is centered on the respective grid node. In the Appendix we determine the suitable range of the spread function for the V_P and V_P/V_S models.

The V_P model is superior to the V_P/V_S model because the *P* arrival times are about 88% of the data set. Nonetheless, the V_P/V_S model is included because it is the only available V_P/V_S model, provides additional information, and has satisfactory values of the spread function, as described below and in the Appendix.

Results

Preferred V_P Model

The preferred 3-D V_P model (LA1-10) of the central Transverse Ranges and the Los Angeles basin successfully images the basin sediments juxtaposed to the bedrock outcrops in the mountains (Figures 3a and 3b). The 2.5 and 3.0 contours for the spread function outline the resolved parts of the model. Because the V_P values of the grid nodes along the edges of the model are held fixed, the resolved parts of the model fall within the outermost nodes of the grid. The spread function contours show that most parts of the model are well resolved down to depths of 20 km, with resolution ranging from 0.2 to 0.8 (see also Appendix). The values of the spread function increase as the values of resolution decrease rapidly between the 3.0 contour and the edges of the model. In particular, offshore to the southwest the spread function is greater than 3.0 and the resolution is poor, less than 0.3.

At 1 km depth the V_P velocity has average values of 4.6 km/s with values from 1.9 to 6.3 km/s, with one extreme value of 6.8 km/s in the Santa Monica Mountains. Although this one value of 6.8 km/s is within a well-resolved part of the model, it is hard to explain in terms of geology and could be an artifact. The San Gabriel and Santa Monica Mountains as well as the Palos Verdes Peninsula are characterized by 5.0 to 6.3 km/s velocities at 1 km depth. In contrast, the sediments of the Ventura and Los Angeles basins have low velocities of 1.9 to 4.0 km/s similar to what *Real* [1977] found by analyzing sonic logs and the geology-based velocity model by *Magistrale et al.* [1996]. There are three areas within the Los Angeles basin, Santa Monica, Long Beach, and the San Gabriel Valley, that have relatively low V_P less than 2.5 km/s at 1 km depth. The spread function values of less than 3.0 indicate that these low V_P anomalies are real and not artifacts of the particular earthquake and source combinations. All of these areas of low near-surface V_P coincide with areas of Holocene sediment deposition and are also consistent with local geological processes.

The size of the variance of V_P for each grid layer decreases as a function of depth (Figure 3). At depths of 16.0 and 20.0 km, the average velocity has reached values of 6.5 and 6.7 km/s. This increase in absolute velocity and decrease in model variance with depth is consistent with what we expect from decreasing material heterogeneity with increasing confining pressure and burial of geological materials.

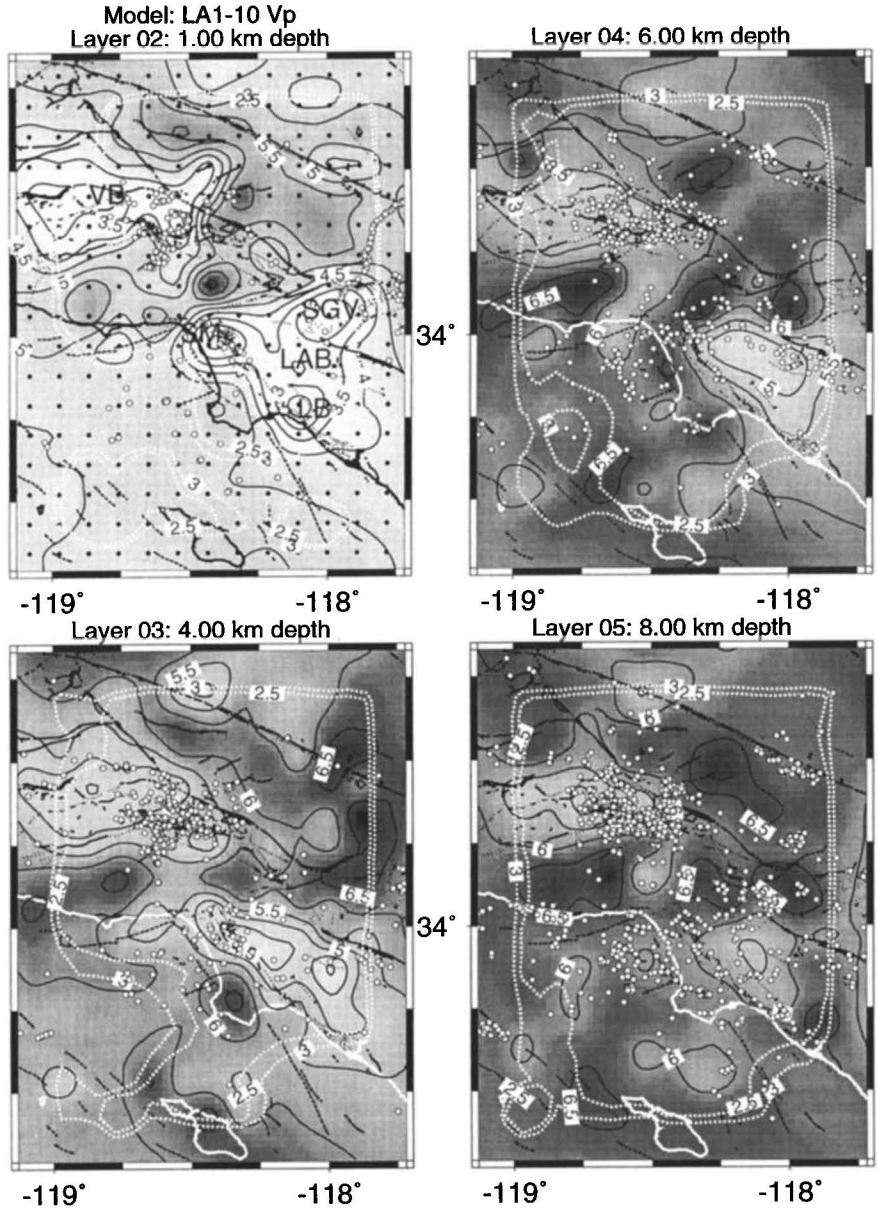

Figure 3a. The final 10 km grid gradational V_p model (LA1-10) shown in four depth slices at depths of 1, 4, 6, and 8 km depth. The 1 km depth slice shows the velocity grid points. For orientation major faults, hypocenters of earthquakes that are within the depth range of each slice and used in the inversion (open circles), and the spread function for 2.5 and 3.0 (dashed white lines) are also shown. SGV, San Gabriel Valley; LB, Long Beach; LAB, Los Angeles basin; VB, Ventura basin.

Preferred V_P/V_S Model

The most prominent changes in the preferred V_P/V_S 3-D model are within and beneath the east Ventura basin, in the north Los Angeles basin, and beneath Santa Monica bay (Figure 4). The overall spatial variations in V_P/V_S range from 1.45 to 2.27.

Although the model is adequately constrained by the data, it should be interpreted carefully (see also Appendix). The 3.0 and 4.0 contours of the spread function are used to evaluate the resolution of the V_P/V_S model. These are higher values than were used for the V_P model because there was a much smaller data set available to constrain the V_P/V_S model. In map view the V_P/V_S model is adequately resolved except offshore to the southwest.

The quality of the arrival time data can affect the spatial variations in the V_P/V_S. The quality of the S arrival times is lower than the P data because in many cases the S arrivals are picked from vertical sensors and in some cases the P coda in the basins or S to P conversions can obscure the true S arrival. Precursory phases that may be more common in the basin however, can only explain a decrease but not an increase in V_P/V_S. Thus increase in V_P/V_S is presumably real, while decreases in V_P/V_S could more easily be artifacts caused by secondary early arrivals such as S to P converted phases.

Significant variations in V_P/V_S were imaged within the Northridge aftershock zone by arrival time data recorded at stations with three-component seismometers deployed following the 1994 Northridge earthquake. These

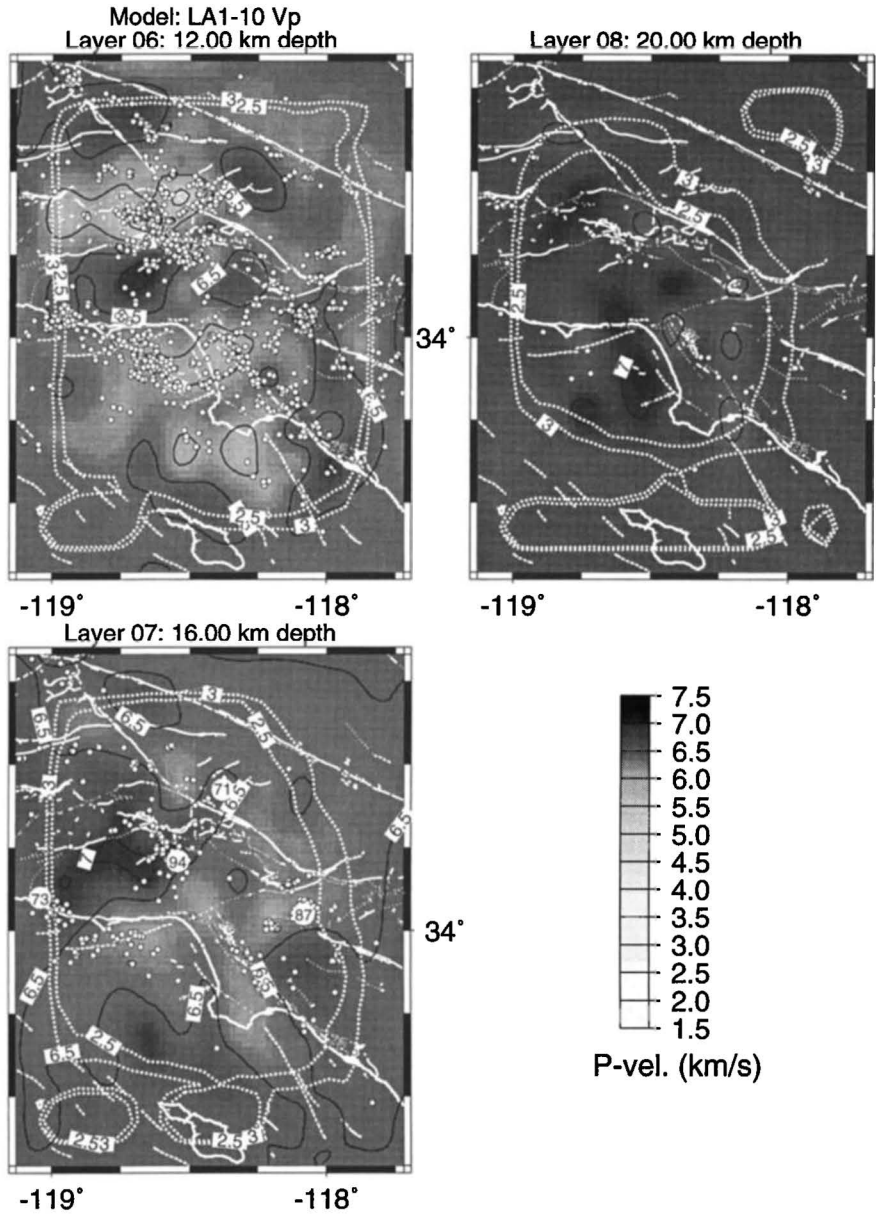

Figure 3b. The final 10 km grid gradational V_p model shown in three depth slices of 12, 16, and 20 km depth. In the 16 km depth section the hypocenters for the 1971 San Fernando, 1973 Point Mugu, 1987 Whittier Narrows, and 1994 Northridge earthquakes are shown. See Figure 3a for details.

variations were noted in earlier studies such as by *Hauksson et al.* [1995], who used an unusually high average V_P/V_S of 1.78 for relocating the Northridge earthquake sequence. In comparison, *Hauksson* [1990] used 1.73 as average value for relocating the seismicity in the Los Angeles region. These variations form the best resolved part of the V_P/V_S model, with spread function values as low as 2.0. The near-surface V_P/V_S are high, reaching a maximum of 2.27 and indicating the presence of water-saturated cracks or high pore fluid pressures in the near surface [*Christensen,* 1996].

Comparison With Superblock Model

To evaluate how the new 3-D V_P model compares to models determined in other studies, we averaged the V_P at grid nodes within three geological areas, Ventura Basin, San Gabriel Mountains, and the Los Angeles basin, and compared them with the superblock model determined by *Magistrale et al.* [1992]. They inverted for average block velocities in major geological regions such as the Los Angeles basin, Ventura basin, and the San Gabriel Mountains (Figures 5a, 5b, and 5c).

Overall, the models are similar when the two standard deviation error bars are taken into account, even though the Magistrale et al. superblocks are averages over fairly large regions. The Ventura basin models exhibit the basic feature of low near-surface and upper-crustal velocities floored by high midcrustal velocities. The Los Angeles basin models differ from the Ventura models in that they do not have anomalously high mid-crustal velocities. The velocities from the Magistrale et al. models are somewhat lower in the near surface in both of the basins. This is not surprising because Magistrale et al. adjusted the top layer

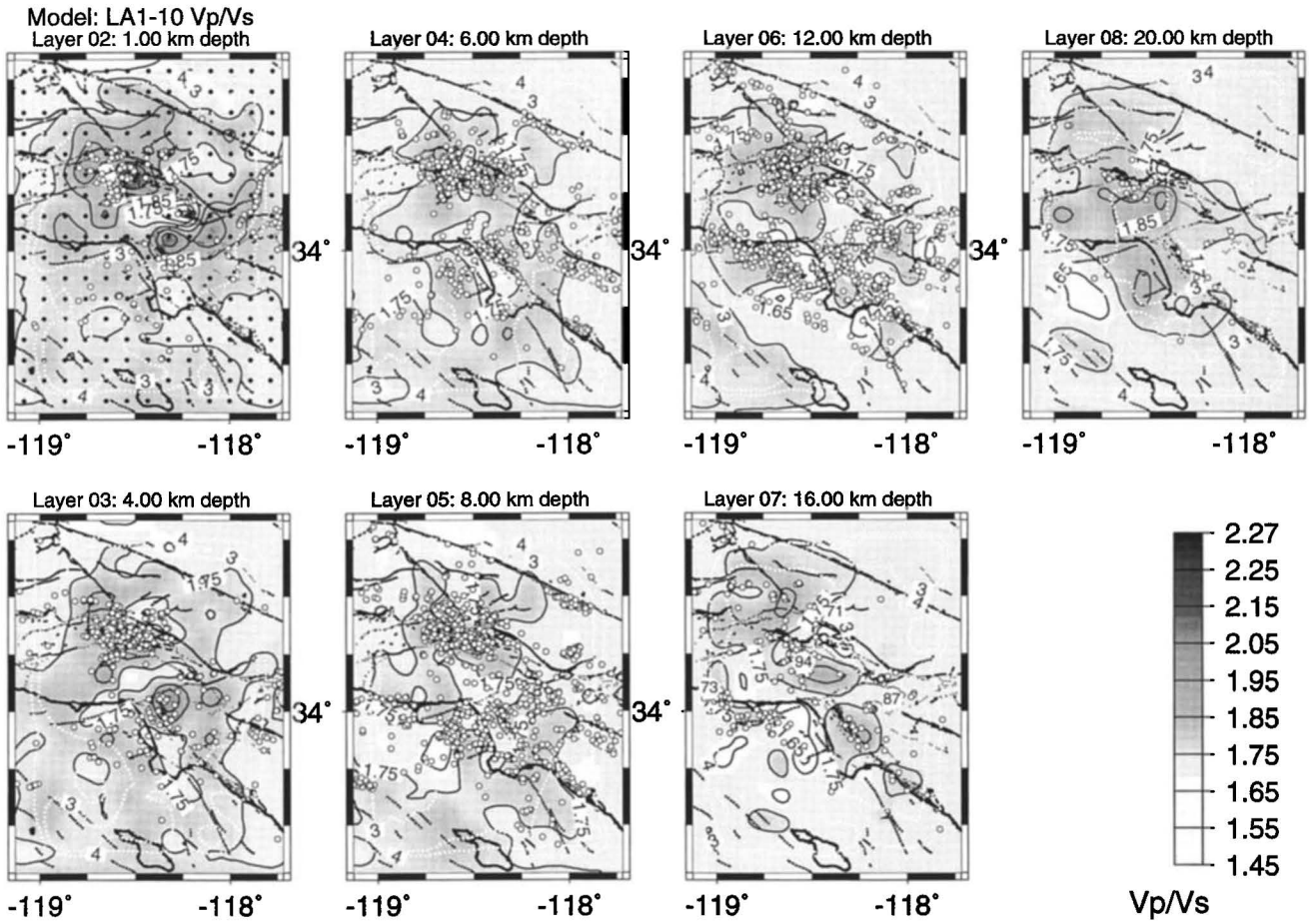

Figure 4. The final 10 km grid gradational V_P/V_S model shown in seven depth slices at depths of 1, 4, 6, 8, 12, 16, and 20 km depth. The 1 km depth slice shows the velocity grid points. Major faults, hypocenters of earthquakes used in the inversion (solid circles), and the spread function for 2.5 and 3.0 (dashed white lines) are also shown.

of their initial model to fit the available shot arrival times as well as possible before the 3-D inversion was done. In contrast to the two basins, the San Gabriel Mountains show high velocities at the surface. The San Gabriel Mountains and the Los Angeles basin have similar average V_P in the depth range of 10 to 20 km. The overall agreement between the models derived with these two different approaches shows that the 3-D model presented here has large-scale features that are consistent with previous studies.

Alternative Initial Model

To test how the final model depended on the initial model, we chose a typical Los Angeles basin model as an endmember slow-starting model and repeated the inversion. The alternative 3-D model, referred to as model LA3-10, is similar to the preferred 3-D model (Figures 5d, 5e, and 5f). Both the Los Angeles basin and Ventura basin depth profiles have similar shape and average velocities within ±0.1 to ±0.2 km/s. The San Gabriel Mountains profiles show the biggest difference, exhibiting two different low-velocity zones at 6-8 km and 14-17 km depth. In the average starting model the shallow low-velocity zone is small or less than 2%, while based on the Los Angeles basin starting model the shallow low-velocity zone becomes more significant, or about 8%. The deep low-velocity zone remains about the same, or about 2%.

The overall similarities between the two 3-D models indicate that the inversion is stable and can be used to get an independent error estimate for the 3-D models. In most cases the final models differ on the average by less than ±0.1 km/s, indicating that this value may be an average uncertainty. At 6 km depth, however, the difference in the San Gabriel Mountains is largest or 0.4 km/s, indicating that the inversion is not restoring successfully the high V_P of the mountains. Further, the final LA3-10 model is inferior to the LA1-10 model because it had a higher final data variance of 0.02445 s^2 (see also Table 1).

Relocations of Shots

To test the validity of the final 3-D model, we have used the 3-D model to redetermine the hypocenters for the 53 shots that were included as part of the inversion. As discussed above, the true locations and origin times of the shots were measured in the field (Figure 2c). The mislocation errors of shots that were located within the San Gabriel Mountains are small, less than 1 km (Figures 6a, 6b, and 6c). The shots located in the San Gabriel Valley

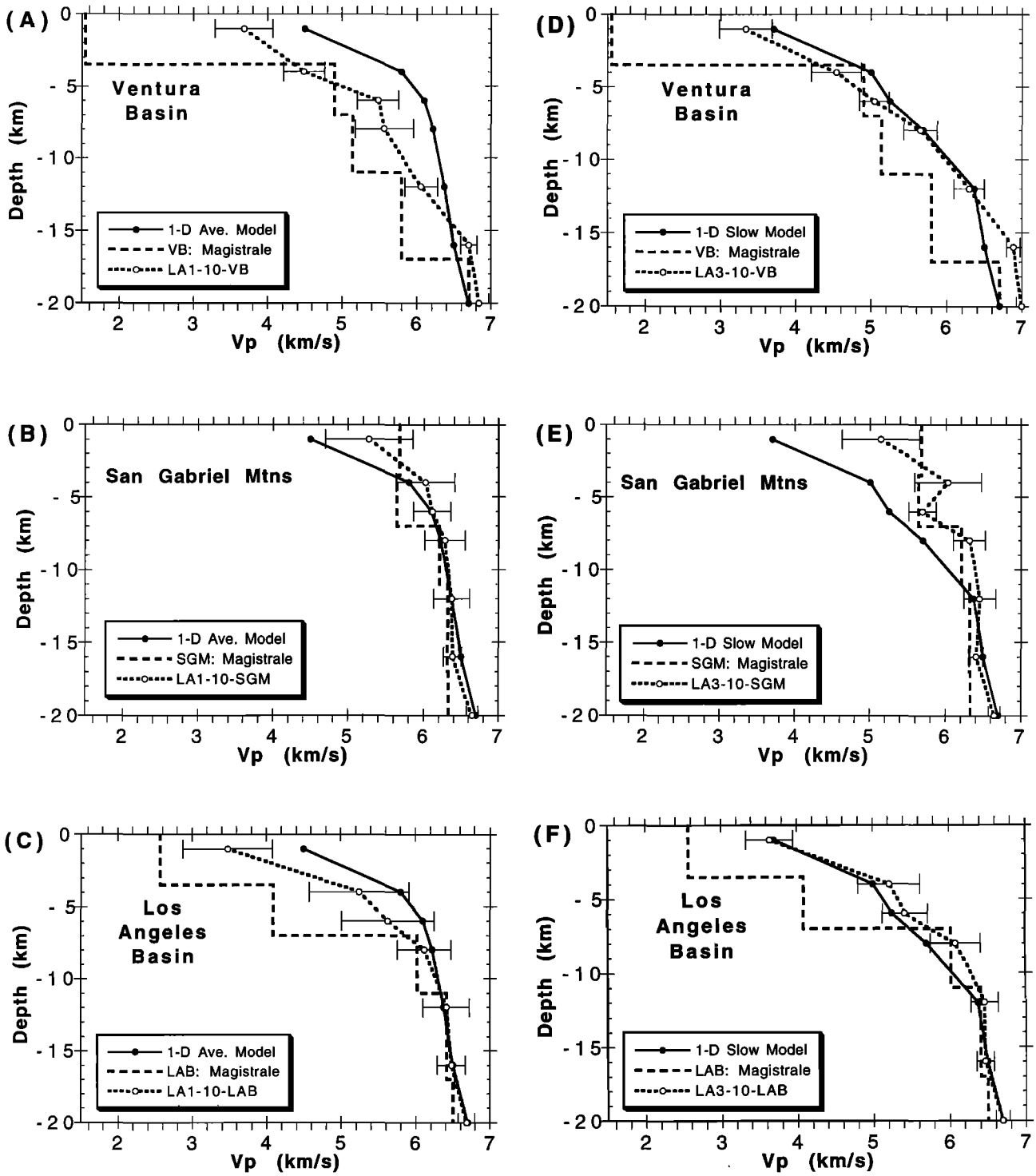

Figure 5. Velocity versus depth profiles for the east Ventura basin, the Los Angeles basin, and the San Gabriel Mountains. Shown are 1-D velocity profiles of the starting model (1-D Ave. Model), the final 3-D model (LA1-10) averaged, including two standard deviations, over regions as defined by superblocks in the models determined by *Magistrale et al.* [1992], which are also shown. (a, b, and c) Standard initial model from *Hauksson et al.* [1995]. (d, e, and f) Slow Los Angeles basin type initial model shown in Figure 5c.

and the Los Angeles basin are mislocated by 1 km and in rare cases by up to 2.5 km. Similarly, the shots located in shallow sedimentary basins in the Mojave Desert are mislocated by up to 2.5 km. These mislocations (up to 2.5 km) could be caused by the sharp velocity contrast between the basin sediments and the hard rock outcrops in the mountains, which makes it difficult to trace rays between the source and receivers. The large mislocations that are observed at the edges and within the basin do not appear at the edges of the model. For instance, the quarry

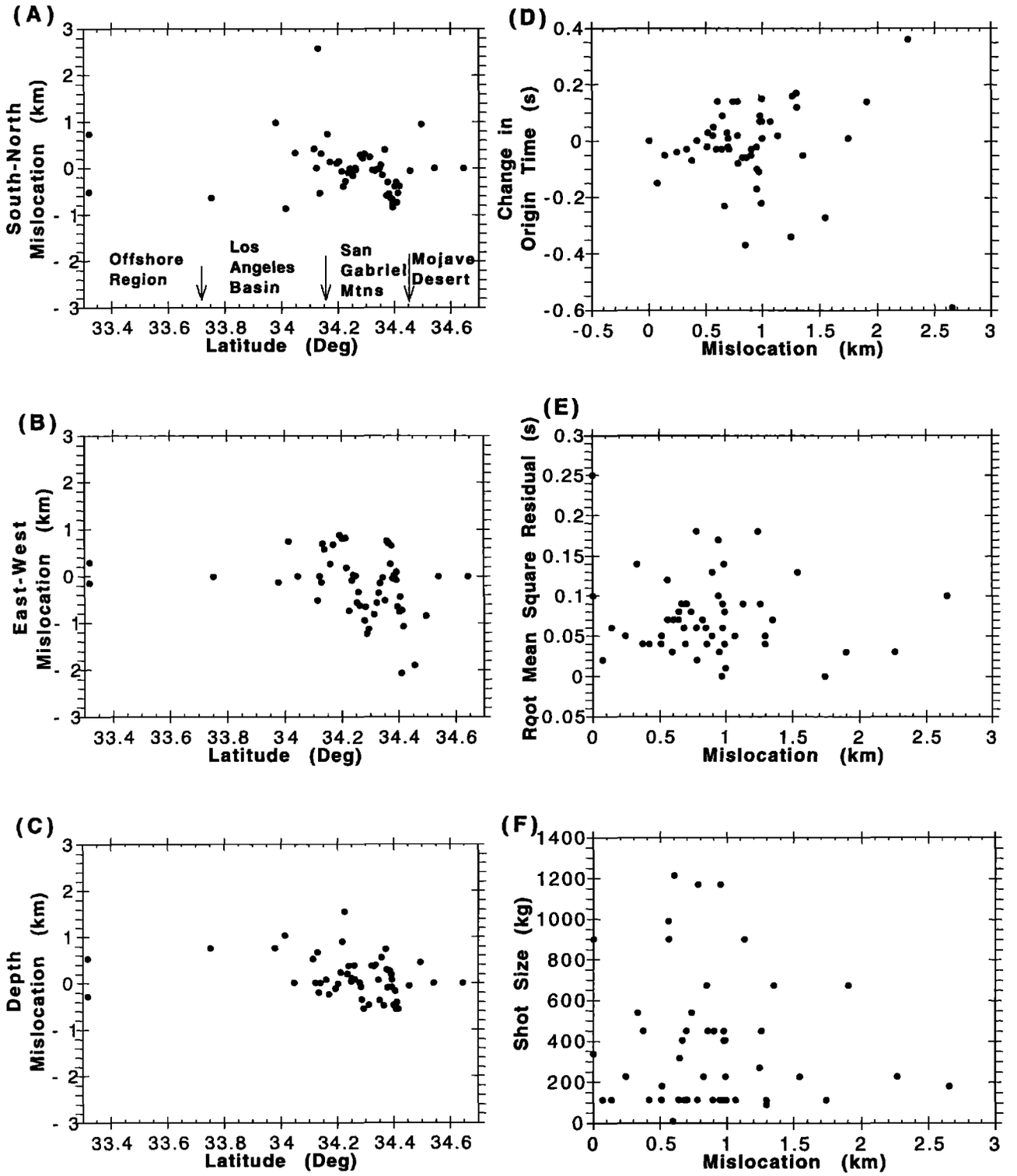

Figure 6. Overview of the 3-D location of the shots. (a) North-south mislocation versus latitude, (b) east-west mislocation versus latitude, (c) depth mislocations versus latitude, (d) change in origin time versus total mislocation, (e) root-mean-square (RMS) error versus mislocation, and (f) shot size versus mislocation.

shots on Catalina Island are mislocated by less than 0.8 km even though they are at the southern edge of the 3-D model. These mislocation errors are upper bounds because most earthquakes would have focus at depth and have many more arrival times to constrain their hypocenters.

Both the variations in shot origin time and root-mean-square (RMS) residuals show mostly random errors indicating that the blast mislocation errors are also random (Figures 6d, 6e, and 6f). The total hypocentral errors are not obviously correlated with shot size, although the shot

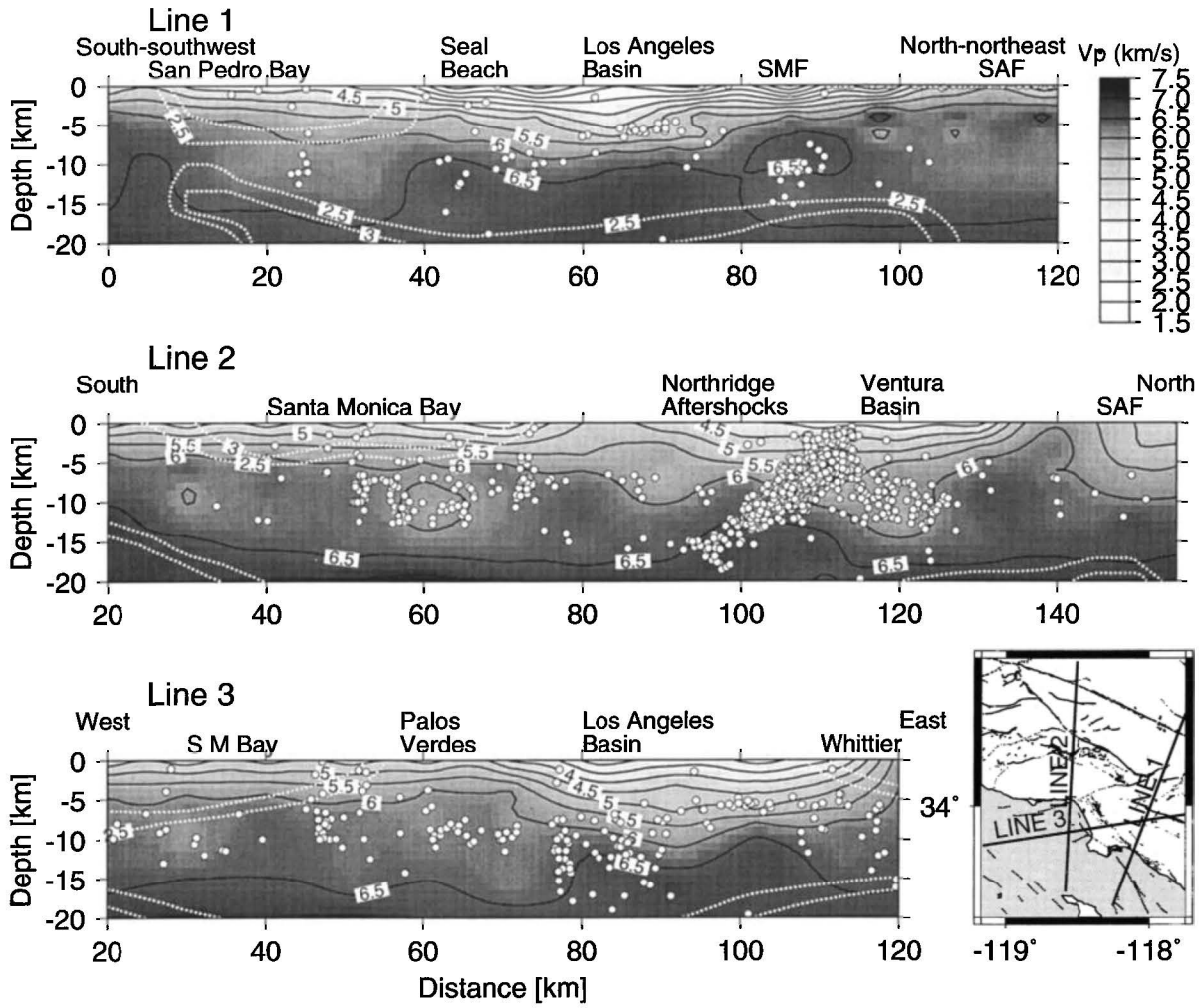

Figure 7. The depth cross sections through the 10 km gradational V_P model along LARSE lines (top) 1, (middle) 2, and (bottom) 3 [*Fuis et al.*, 1996]. Hypocenters used in the inversion and located within 5 km distance of each cross section are also shown. The dashed white lines are the values of the spread function. Map at bottom right shows location of the profiles. SMF, Sierra Madre fault; SM, Santa Monica; SAF, San Andreas fault.

size ranged from 9 kg to more than 1170 kg. Shots of 9 kg or less were not adequately recorded by the SCSN to allow relocation.

Geological Interpretations

The 3-D V_P and V_P/V_S models provide new images of the large-scale geological structures such as mountains and basins. They also image a number of small-scale structural features that were previously only inferred or unknown.

Regional 3-D Structures

The depth variations of V_P, V_P/V_S, and V_S across the study region illuminate the basin shapes, their basement structure, as well as the structure beneath the mountain ranges at intermediate depth (Figures 7, 8, and 9). The shallow offshore basins such as the Santa Monica Bay or San Pedro Bay basins are not adequately resolved by the SCSN arrival times alone. The offshore structures at depths below about 5 km, however, are well resolved.

There are four major ridges of high-velocity material as defined by the V_P 6.5 km/s contour. All of these ridges involve more than one grid node, fall within the region of low values of the spread function, and consist of more than one layer of grid nodes, suggesting that their shape is well defined.

The first ridge beneath the San Gabriel Mountains that is in the depth range of 5 to 20 km is characterized by discontinuous blocks of high-velocity material. Some of these blocks may be detached and thus underlain by low-velocity zones. This structural style was also found by *Fuis et al.* [1996] who analyzed the LARSE refraction data.

The second ridge, defined by the V_P 6.5 km/s contour, rises beneath the Santa Monica Mountains extending from west to east for a distance of at least 70 km. This structure is more continuous than the San Gabriel Mountains structure and is only interrupted by low-velocity material due north of Santa Monica.

The third ridge that is located beneath and to the east of the Los Angeles basin is most likely the northernmost extension of the Peninsular Range batholith. This ridge

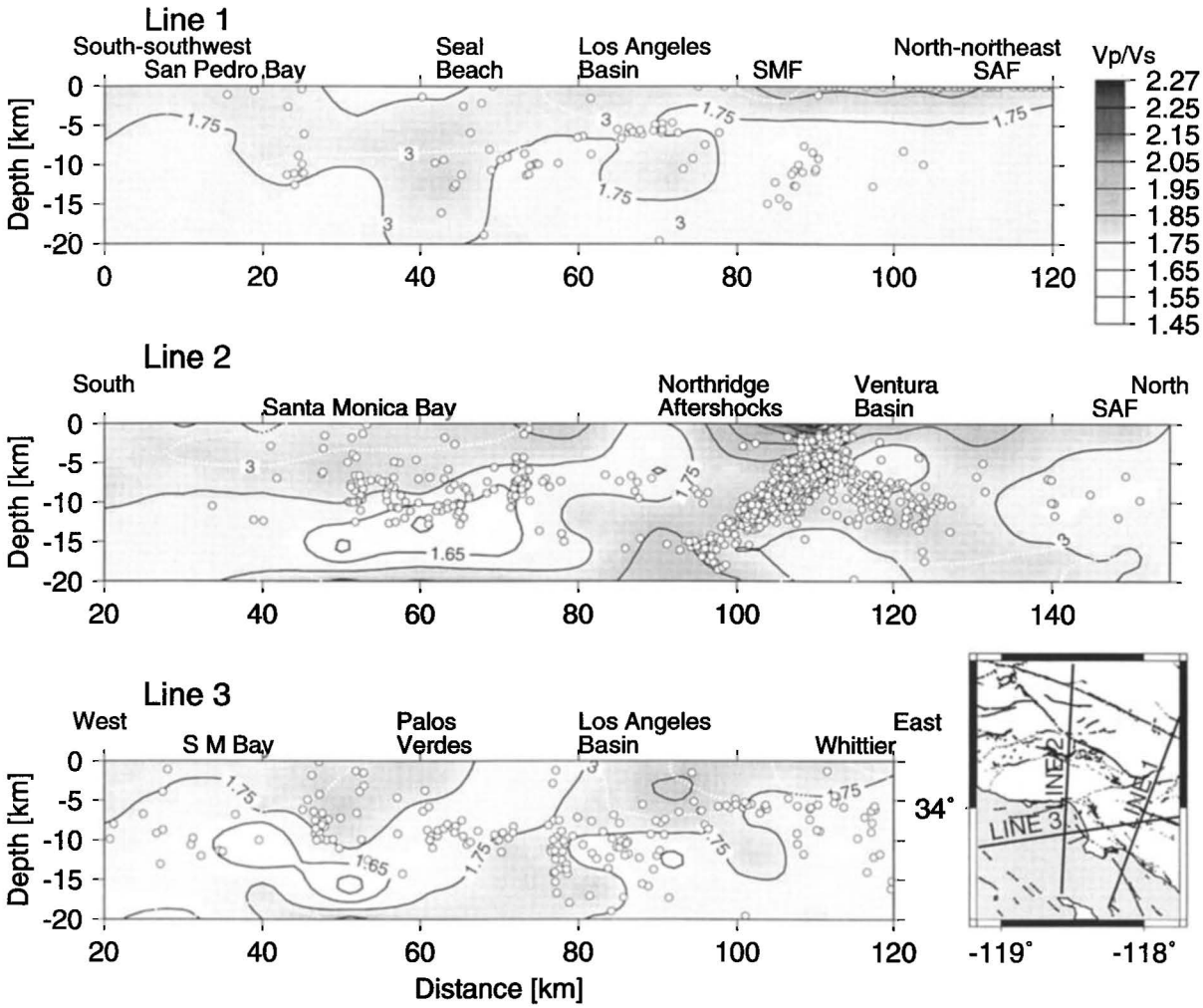

Figure 8. The depth cross sections through the 10 km gradational V_P/V_S model along LARSE lines (top) 1, (middle) 2, and (bottom) 3. Hypocenters used in the inversion and located within 5 km distance of each cross section are also shown. The dashed white lines are the values of the spread function. Map at bottom right shows location of the profiles. SMF, Sierra Madre fault; SM, Santa Monica; SAF, San Andreas fault.

may be flanked be Catalina Schist to the south and Pelona Schist to the north. *Magistrale and Zhou* [1996] analyzed the depth distribution of southern California earthquakes and argued that the Catalina and Pelona schists become plastic at lower temperatures than the more feldspar rich basement rocks of the Peninsular Ranges. Some of this effect can be seen in Figure 7 where seismicity is about 5 km shallower to the west than to the north of the Newport-Inglewood fault.

The fourth ridge that is characterized by both high V_P and V_P/V_S in the depth range of 12-20 km beneath the western Santa Monica Mountains, the Simi Hills, and the Santa Susana Mountains, may be indicative of fragmentation and mixture of pieces of quartzitic continental and mafic oceanic crust [e.g., *Christensen and Mooney,* 1995]. In addition, *Christensen* [1996] showed that for ophiolites the V_P/V_S ratio ranges from 1.88 to 1.89, indirectly supporting the idea that the Ventura basin and the region to the southwest are floored by ophiolitic sequences. The hypocenter of the 1994 M_W 6.7 Northridge earthquake is located within this zone of high V_P and V_P/V_S. *Thurber and Atre* [1993] found a similar zone of high V_P and V_P/V_S at both shallow and greater depths of 16 km along the 1989 (M_W 6.9) Loma Prieta rupture zone. They also attributed the high V_P/V_S to the presence of mafic rocks.

Near-surface lateral spatial variations in V_P/V_S are mostly confined to the Ventura and the north Los Angeles basin. In the east Ventura basin the high V_P/V_S of 1.8 to 2.25, centered on the basin, is most prominent and extends to depths of 8 km. A localized 1 km deep anomaly of low V_P/V_S coincides with high V_P to the west of the Verdugo Mountains and separates the Ventura basin from the high V_P/V_S in the north Los Angeles basin. Both of these anomalies are well resolved because they are located within the 3.0 spread function contour.

The high V_P/V_S at depths shallower than 1 km or above the top layer in this model have been documented in previous studies. For instance, using travel times from a borehole array located in the northwest corner of the Los Angeles basin, *Hauksson et al.* [1987] found V_P/V_S of 3.4 in the depth range from 0 to 420 m and a lower ratio of 1.7

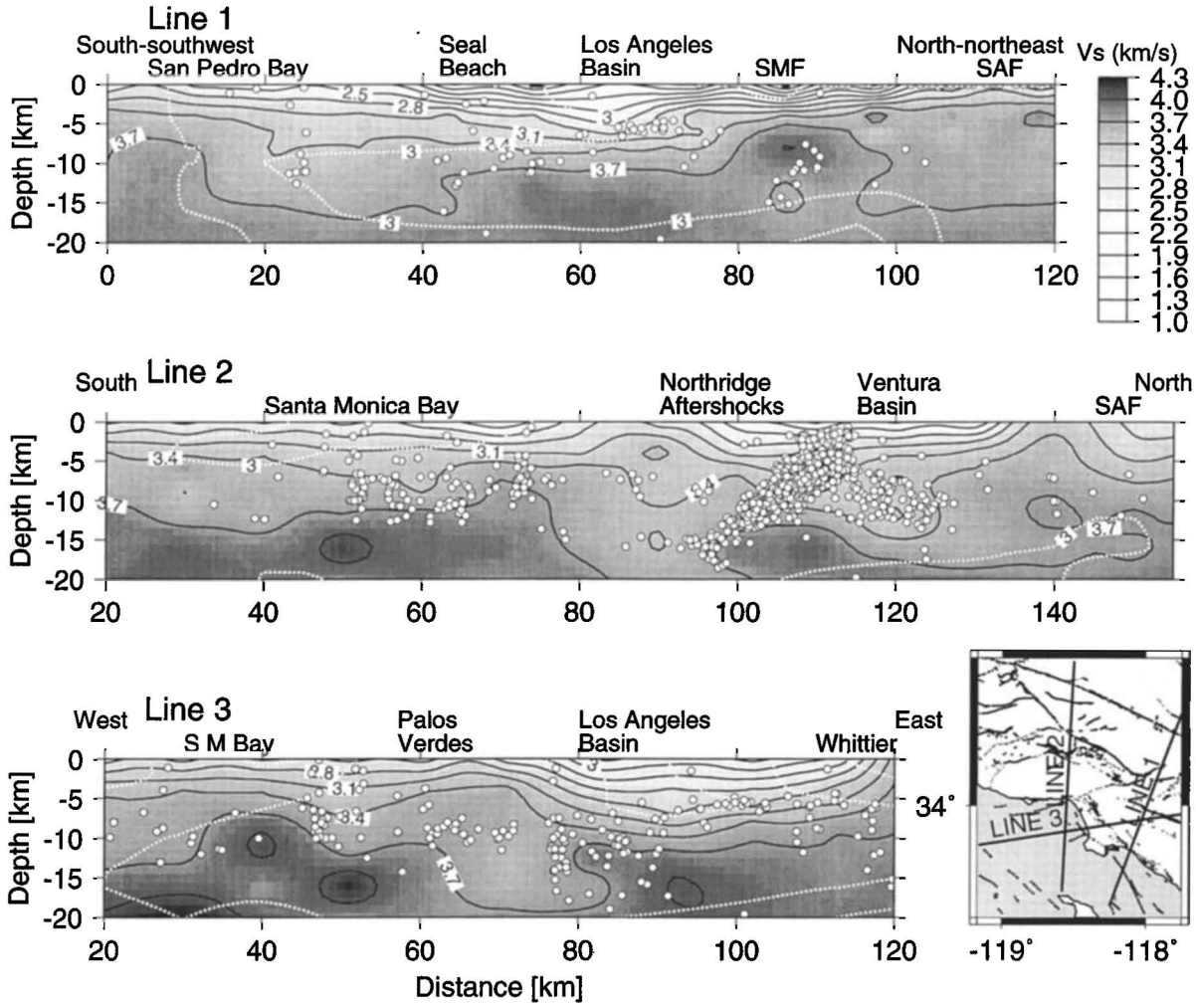

Figure 9. The depth cross sections through the 10 km gradational V_S model along LARSE lines (top) 1, (middle) 2, and (bottom) 3. Hypocenters used in the inversion and located within 5 km distance of each cross section are also shown. The dashed white lines are the values of the spread function. Map at bottom right shows location of the profiles. SMF, Sierra Madre fault; SM, Santa Monica; SAF, San Andreas fault.

in the depth range of 420 to 1500 m. Similarly high V_P/V_S ratios have been found in the near-surface of the eastern Transverse Ranges in southern California [*Nicholson and Simpson,* 1985].

Beneath Santa Monica Bay, normal V_S and a prominent low V_P/V_S anomaly of 1.65 exist in the depth range of 8 to 16 km (Figure 9). We do not consider this anomaly to be the effect of mislocated offshore earthquakes, because it is within a region that is satisfactorily covered by stations on the Palos Verdes Peninsula and in the Santa Monica Mountains. Furthermore, the anomaly does not become more pronounced with increasing distance, suggesting that it is not an artifact. This anomaly that has a lateral extent of about 20 by 30 km appears to be surrounded by regions of intermediate V_P/V_S and ongoing background seismicity [*Hauksson and Saldivar,* 1989].

Los Angeles Basin

We compare the 3-D V_P model (Figure 10) with the mostly northeast striking geological cross sections from *Wright* [1991]. At shallow depth where the geological data and the 3-D model overlap, the overall agreement between the 3-D model and the geological data confirms the validity of the 3-D V_P model. Furthermore, the information provided by the 3-D model at greater depths, beneath the geological cross sections, allows us to infer the structure of the Los Angles basin basement, in more detail than was available before.

The west and east sides of the Los Angeles basin coincide with the high V_P on the far side of the Newport-Inglewood and Whittier faults. The basin sediments have V_P ranging from 1.9 km/s at the surface to 5.5 km/s near the bottom of the basin. To the north the basin abuts the high velocities of the Santa Monica Mountains. As can be seen in section BB', there is a suggestion that the Las Cienegas fault separates Catalina Schist from Peninsular Range basement down to depths of at least 15 km. In the south it gradually shallows out against the high velocities of the Peninsular ranges batholith. The earthquake hypocenters outline the major fault structures such as the Newport-Inglewood fault zone and the thrust system,

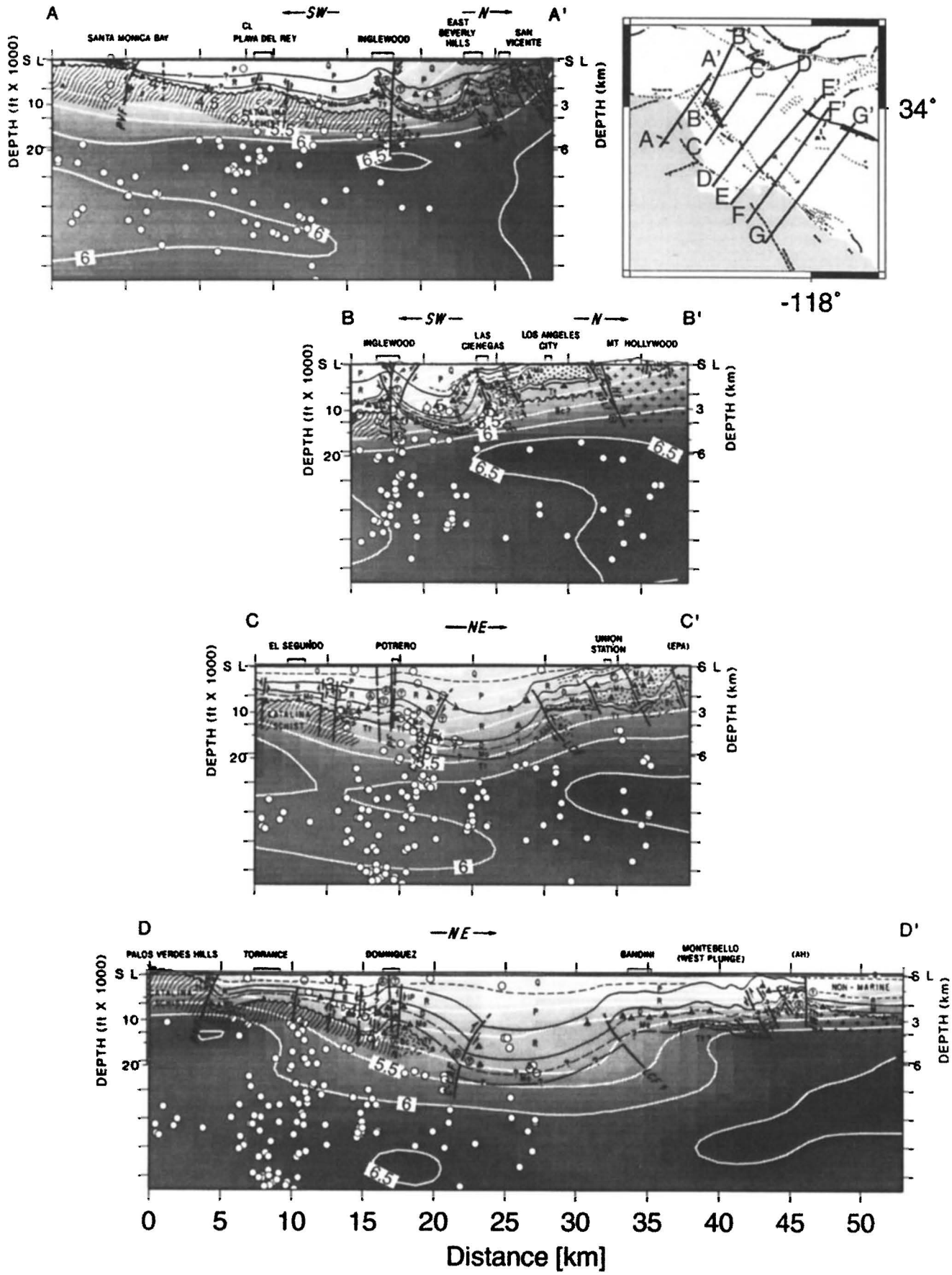
A
SW
N
A'
SANTA MONICA BAY
CL
PLAYA DEL REY
INGLEWOOD
EAST
BEVERLY
HILLS
SAN
VICENTE
S L
DEPTH (ft X 1000)
DEPTH (km)
10
20
3
6
6.5
B
B'
LAS
CIENEGAS
LOS ANGELES
CITY
MT HOLLYWOOD
C
C'
NE
EL SEGUNDO
POTRERO
UNION
STATION
(EPA)
D
D'
PALOS VERDES HILLS
TORRANCE
DOMINGUEZ
SANDINI
MONTEBELLO
(WEST PLUNGE)
(AH)
NON - MARINE
34°
-118°
0
5
10
15
20
25
30
35
40
45
50
Distance [km]

including the Whittier fault, the east flank on the basin. The V_P of the east flank of 6.5 km/s and normal V_P/V_S of 1.75 suggest a granite to granodiorite composition mixed with Mesozoic volcanics and metavolcanic rocks such as diabase [*Christensen and Mooney*, 1995]. In contrast, the west flank is underlain by materials of intermediate velocities that come up to the surface as Catalina schist toward the southwest in the Palos Verdes Hills.

The basin continues to broaden toward Sunset Beach in the south (Figure 10b). The overall width and depth shapes are consistent between the V_P and geological data. At depth the Peninsular Ranges batholith becomes more prominent to the south. As seen most clearly in cross section F-F', the eastern edge of the basin is consistent with the geological data except for the Puente Hills located between the San Gabriel valley and the Los Angles basin, which are not wide enough to be resolved in this study. The Catalina schist that outcrops on the Palos Verdes Peninsula has velocities of 5.5 ± 0.5 km/s and appears to extend beneath most of the basin as a layer of 2 to 6 km thickness.

East Ventura Basin and Northridge Thrust Ramp

To compare the 3-D V_P model with geological features such as basin shapes, major faults, and folds in the east Ventura basin, we have superimposed cross sections from the 3-D velocity model on top of geological sections by *Huftile and Yeats* [1996] and *Davis and Namson* [1994]. The near-surface low velocities in the east Ventura basin beneath the Santa Susana Mountains reflect the basin shape as determined from surficial and borehole data (Figure 11). Using the additional information from the model, the major surficial faults such as Oak Ridge, San Cayetano, and Santa Susana faults can be projected downdip illustrating in a similar way as the geological data how the faults play a role in the deformation of the east Ventura basin. For instance, the sharp uplift of the basement along the south dipping Oak Ridge fault in cross section A-A' is reflected in both the geology and the 3-D V_P model. Also, in cross section B-B' the Santa Susana fault is associated with a zone of low velocity that is being underthrust beneath higher-velocity material.

Both the thrust focal mechanism of the 1994 M_W 6.7 Northridge earthquake and the surficial deformation suggest the presence of a thrust ramp at depth [e.g., *Hauksson et al.*, 1995; *Yeats and Huftile*, 1995]. The Northridge thrust ramp is associated with a much smaller bulge in the 6.0 and 6.5 km/s velocity contours than the Santa Susana fault, suggesting that the Northridge ramp has had significantly lower cumulative offset than the Santa Susana fault. This observation is consistent with the larger offset on the Santa Susana fault [*Huftile and Yeats*, 1996], demonstrating agreement between the surficial geological data and the 3-D velocity model.

A more detailed image of the Northridge thrust ramp is shown in the *Davis and Namson* [1994] and *Davis et al.*, [1996] cross section located a few kilometers to the east of the Yeats cross section (Figure 12). The Davis and Namson cross section includes, along with the geological and borehole data, a fault-propagation fold interpretation. This interpretation is used by Davis and Namson to explain the origin of major basement cored folds, to extrapolate surficial faults downdip, and to identify concealed faults such as the Northridge thrust ramp. The superposition of their cross section on the 3-D velocity model and the 3-D relocations of the hypocenters shows some consistencies. The overall basinal shape in the near surface is reflected in both data sets. Some parts of the velocity model are consistent with the predictions of the fault- propagation fold model, such as the rise of the 6.5 km/s contour to shallower depths to the south, beneath the Santa Monica Mountains.

A major feature of the fault-propagation fold interpretation by *Davis and Namson* [1994] is a subhorizontal detachment at 19 km depth (Figure 12). Although the Davis and Namson model does not require a significant velocity contrast across the sub-horizontal detachment at depth, it is worth noting that no significant velocity contrast can be identified. This observation suggests that the presence of a detachment surface at depth may be more controlled by the depth of the brittle-ductile transition zone than the presence of a lithological contrast. Alternatively, the postulated detachment surface is located deeper or below 20 km depth, the bottom of the model.

Discussion

Los Angeles Tectonics

The central Transverse Ranges and the Los Angeles basin form a complex region of transitional crust [*Crouch*

Figure 10a. Geological cross sections A-A' through D-D' and parts of this caption from *Wright* [1991 reprinted by permission of the American Association of Petroleum Geologists]. Superimposed are the 3-D V_P velocity cross sections and hypocenters used in the inversion as open circles. Location map shown in top right corner of Figure 10a. Cross sections are centered on Newport-Inglewood fault zone. Solid triangles (and letters below) indicate location and total depth of control wells [*Wright*, 1991]. Arrows on faults indicate dip slip. Circled letters show lateral fault motion: A, away from reader; T, toward reader (thus A/T is right slip, T/A is left slip). Abbreviations: CHF, Cherry Hill fault; IF, Inglewood fault; LCF, Las Cienegas fault; NF, Norwalk fault; NSLF, North Salt Lake fault; PF, Potrero fault; RSZ ,"Regional shear zone"; WoHF, Workman Hill fault; WF, Whittier fault; PVF, Palos Verdes fault; PHT, Peralta Hills fault; SCF, Shady Canyon fault; SL, sea level; CL-coastline. Light dashed lines are subordinate stratigraphic boundaries from *Wright* [1991]. Q, Quaternary; P, Pico Formation; R, Repetto Formation; D, Delmontian; Mo, Mohnian; M, undifferentiated Delmontian-Mohnian; Tm, Monterey Formation; L, Luisian; v, volcanics; Tt, Topanga Formation; Pg, Paleogene (locally includes lower Miocene); K, Cretaceous, Bc, undifferentiated metaphoric basement complex; and u, m, and l, upper, middle, and lower, respectively. Stippled unit is middle Mohnian Soquel/"Massive" sandstones.

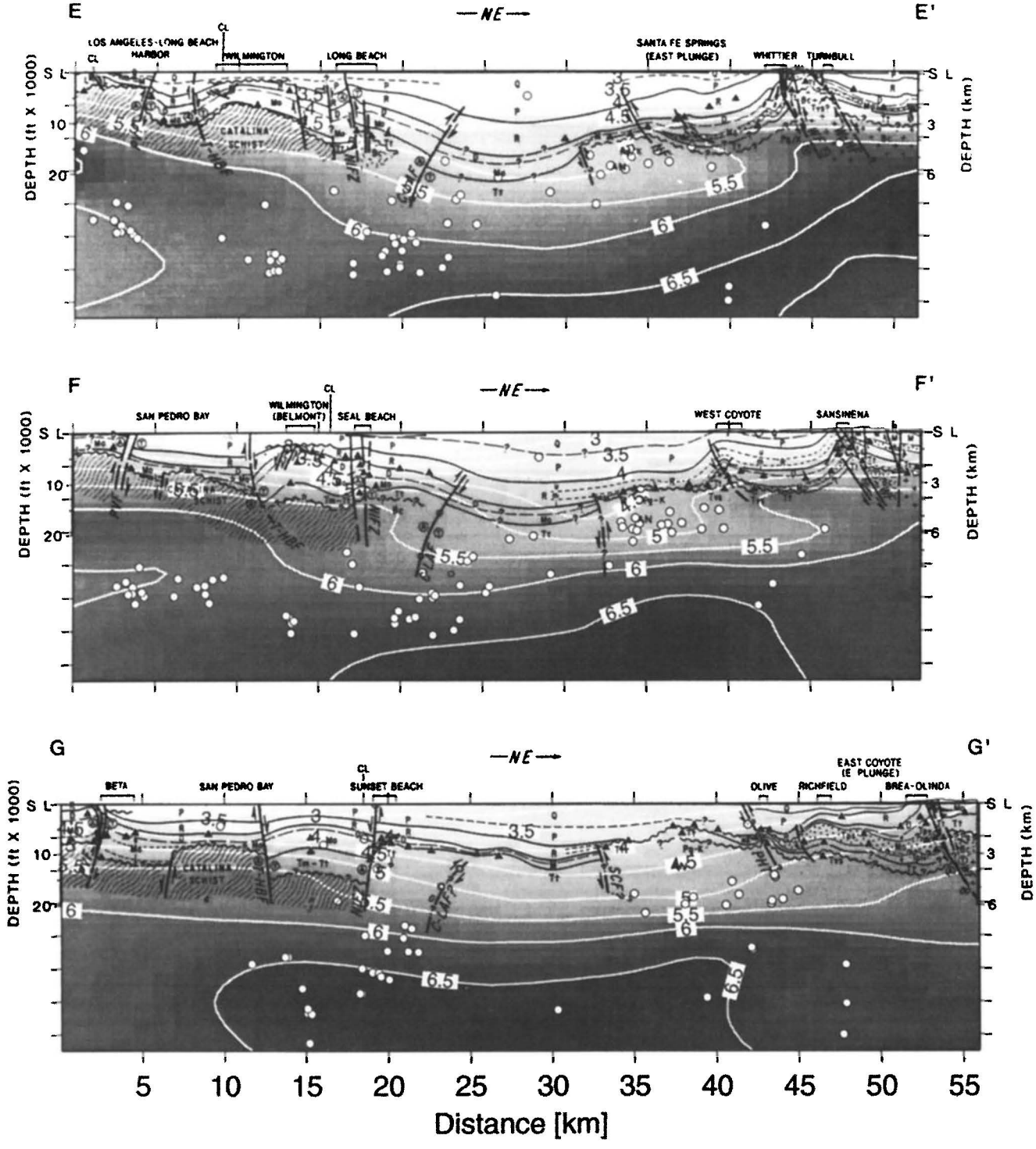

Figure 10b. As in Figure 10a, except for geological cross sections E-E' through G-G'.

Figure 11. (opposite, top and middle) Cross sections through the 10 km grid gradational V_P model along geological structural cross sections by *Huftile and Yeats* [1996 reprinted by permission of the Seismological Socity of America]. Hypocenters used in the inversion are shown as white open circles. (bottom) Map from *Huftile and Yeats* [1996] showing location of the profiles. Geology as follows from *Huftile and Yeats* [1996]: ABF, Agua Blanca fault; CLR, Chatsworth lateral ramp; DVF, Del Valle fault; GCL, Gillibrand Canyon lateral ramp; GHF, Granada Hills fault; HRA, Hopper Ranch-Modelo anticline; NHF, Northridge Hills fault; NPA, Newhall-Potrero anticline; PA, Pico anticline; SFF, San Fernando fault. Stratigraphic nomenclature, see *Huftile and Yeats* [1996].

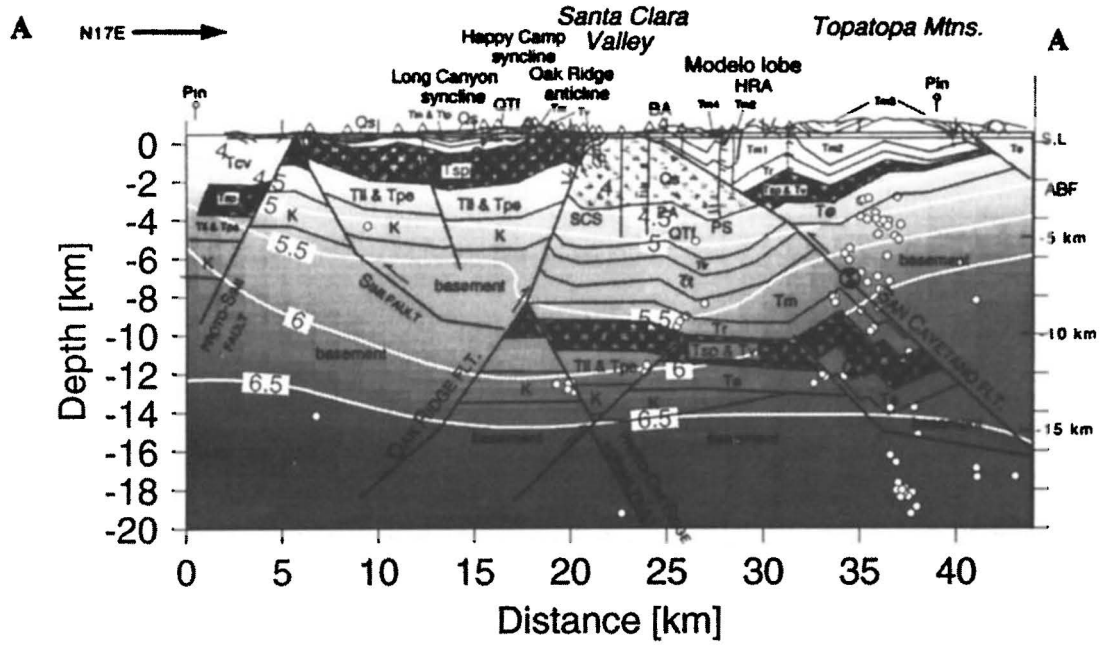
A
N17E
Santa Clara Valley
Topatopa Mtns.
Happy Camp syncline
Long Canyon syncline
Oak Ridge anticline
Modelo lobe
HRA
Pin
S.L
ABF
5 km
10 km
15 km
basement
Sierra Madre FAULT
Oak Ridge F.T.
San Cayetano F.T.
Depth [km]
Distance [km]

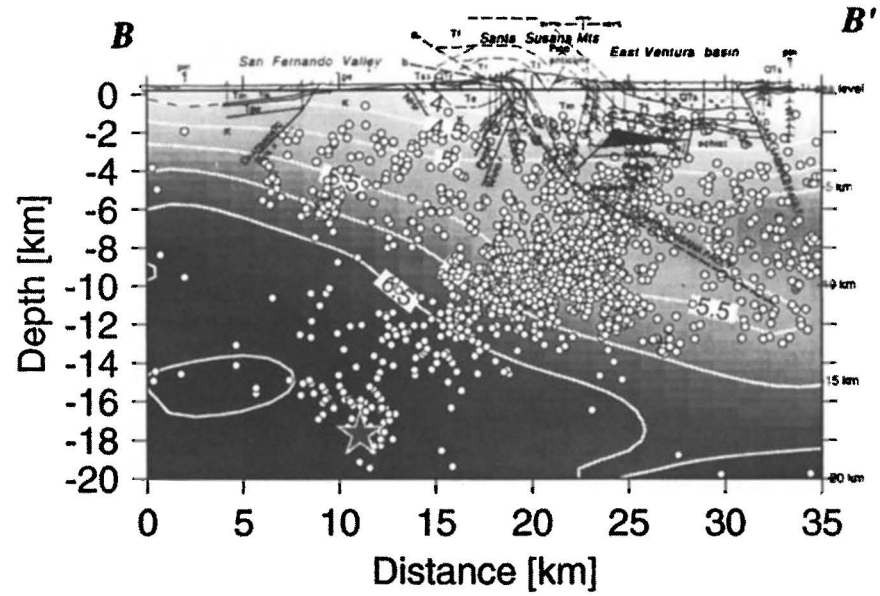
B
B'
San Fernando Valley
Santa Susana Mts
East Ventura basin
Depth [km]
Distance [km]

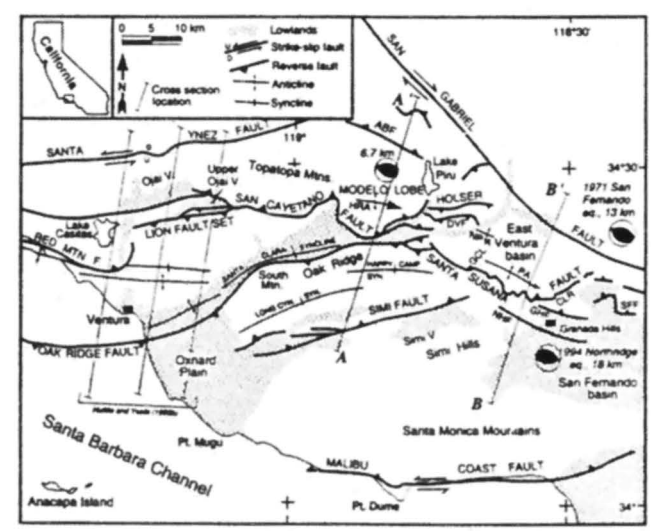
California
Lowlands
Strike-slip fault
Reverse fault
Anticline
Syncline
Cross section location
SANTA YNEZ FAULT
Topatopa Mtns.
SAN CAYETANO FAULT
MODELO LOBE
HOLSER FAULT
East Ventura basin
SANTA SUSANA FAULT
SIMI FAULT
OAK RIDGE FAULT
Oxnard Plain
Simi Hills
Santa Monica Mountains
Santa Barbara Channel
Pt. Mugu
MALIBU COAST FAULT
Anacapa Island
Pt. Dume
1971 San Fernando eq., 13 km
1994 Northridge eq., 18 km
San Fernando basin

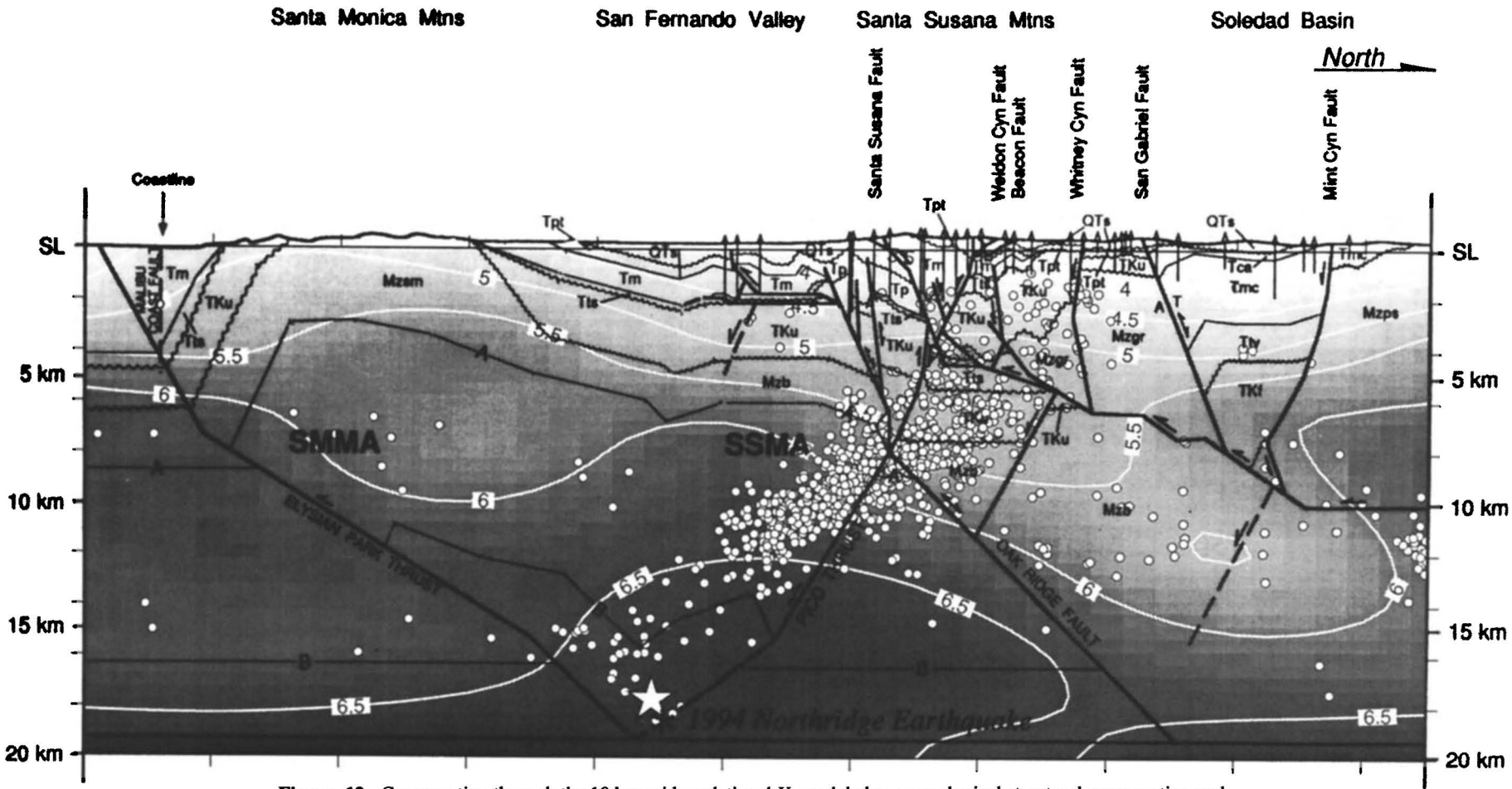

Figure 12. Cross section through the 10 km grid gradational V_P model along a geological structural cross section and parts of this caption by *Davis et al.* [1996 used with permission of the Pacific Section SEPM]. This cross section that also includes fault-bent fault interpretations is located approximately 5 miles to the east of the BB' cross section in Figure 11. Hypocenters used in the inversion are shown as open circles. Segments A-B are lines showing late Cenozoic compressive strain. SMMA, Santa Monica Mountains anticlinorium; SSMA, Santa Susana Mountains anticlinorium. San Fernando valley and Santa Susana Mountains, QTs, Saugus Formation; Tpt, Pico and Towsley Formations; Tm, Monterey and Sisquoc Formations; Tts - Topanga and Sespe Formations; TKu, Undifferentiated Paleogene and Upper Cretaceous age rocks; Mzsm, Santa Monica slate; Mzb, Undifferentiated crystalline rock. Soledad basin, QTs, Saugus Formation; Tca, Castaic Formation; Tmc, Mint Canyon Formation; Ttv, Tick Canyon and Vaqueros Formations; Tkf, San Francisquito Formation; Mzps, Pelona schist; Mzgr, granitic rocks.

and Suppe, 1993]. Oceanic crust lies offshore to the south and west, beyond the continental borderland, and continental crust exists to the north and east. In addition, the complex tectonic history of the region, with extensional tectonics dominating from 20 to 4 million years ago and transpressional tectonics from 4 million to present, has contributed to the overall structural complexity [e.g., *Crowell,* 1987; *Wright,* 1991]. Crustal blocks have also rotated and moved laterally, as demonstrated by paleomagnetic data [*Luyendyk et al.,* 1980]. Prominent surficial evidence for the transitional crust and tectonic deformation are the rugged topography that is crosscut by deep sediment-filled basins.

The new 3-D images of the central Transverse Ranges and the Los Angeles basin provide the third dimension to this complex structure. They illuminate the east Ventura basin and the Los Angeles basin revealing their different geometrical shapes and their juxtaposition to mountain ranges. The east Ventura basin is deeper, narrower, and has on average lower velocities in the basin fill than the Los Angeles basin. As also suggested by *Magistrale et al.* [1992], below 12 km the east Ventura basin is underlain by material of higher V_P and V_P/V_S, suggesting the presence of mafic crust such as ophiolitic sequences [*Sorensen,* 1985; *Crowell,* 1987]. In comparison, the Los Angeles basin to the south is underlain by fragments of the Peninsular Ranges batholith and to the north by similar rocks as found in the San Gabriel Mountains. In addition, the Ventura basin differs from the Los Angeles basin because of the unusually low heat flow and deep earthquakes beneath the basin sediments [*Bryant and Jones,* 1992]. The Ventura basin is also accommodating a higher rate of north-south compression than the Los Angeles basin [*Donnellan et al.,* 1993]. Thus the 3-D velocity models reflect the different origin and tectonic history of the basins.

The 3-D images of the two major mountain ranges, Santa Monica Mountains and the San Gabriel Mountains, also reflect their tectonic structures (Figure 3). The laterally complex ridge structure beneath the San Gabriel and Santa Monica mountain ranges is consistent with models of regional tectonics that involve juxtaposition of diverse terranes linked to Cenozoic transcurrent fault activity [*Silver,* 1995; *Wright,* 1991]. The Catalina Schist and the arc-like rocks like Santa Monica formation, with V_P of up to 7.0 km/s, indicate that some of these structures are from previous tectonic episodes including Mesozoic subduction and arc-forming processes [*Sorensen,* 1985]. The core of the Santa Monica Mountains consists of the 6.5 km/s material that appears to form the top of the lower crust. Some of the uplift of this high-velocity material may indicate ongoing faulting and shortening of the lower crust [e.g., *Yeats,* 1993]. Such uplift occurred in the 1994 (M_W 6.7) Northridge earthquake [*Hauksson et al.,* 1995]. The eastern Santa Monica Mountains that are separated by a zone of intermediate velocity from the western part, have similar V_P at depth as are found beneath the Los Angeles basin, consistent with block rotations in the region as modeled by *Luyendyk et al.* [1980].

When analyzing the vertical distribution of V_P, only the San Gabriel Mountains are characterized by two possible low-V_P zones. The first is at shallow depth of 6 to 8 km and the second is at intermediate depths of 16 to 18 km. Both of these low-V_P zones have been identified in previous studies, including in the superblock model by *Magistrale et al.* [1992]. *Nicholson and Simpson* [1985] using a back stripping technique, identified a low-velocity zone at depths of 8 to 9 km, located in the eastern Transverse Ranges. Using receiver functions from the Pasadena station, *Langston* [1989] also identified a low-velocity zone in the depth range of 16 to 20 km. These structures are also consistent with the low-angle layered plate structure of the range, consisting of cratonic plutonic rocks resting on top of the Vincent gap mylonite zone with Pelona schist at greater depth [*Ehlig,* 1981; *Silver,* 1995]. Because of the presence of these low- velocity zones, the core of the San Gabriel Mountains is characterized by blocks of 6.5 km/s material that are mostly separated from the top of the (6.5 km/s) lower crust.

The spatial variations in V_P/V_S may also have a bearing on the relative importance of aseismic and seismic deformation in the greater Los Angeles region. If aseismic deformation processes such as pressure solution make a significant contribution to the north-south contraction of the region, this might be reflected locally in higher V_P/V_S values [e.g., *Scholz,* 1989]. However, it may be difficult to differentiate between spatial variations in V_P/V_S caused by high fluid pressures or differences in rock chemistry caused by the complex tectonic history of the region.

Evidence for Thrust Ramps and Hanging Wall Deformation

One of the goals of this study was to image structures such as thrust ramps or deformation of the hanging wall associated with concealed thrust faults. Some of the model-based or mapped geological features in the region are shown schematically in Figure 13. The thin- and thick-skinned tectonics indicate the role of the lower crust in the deformation while the basin extension and closure indicate the possible patterns of hanging wall deformation. If such features can be identified in 3-D velocity models, we have an independent means of mapping these structures and hence quantifying their contribution to the tectonic shortening [*Donnellan et al.,* 1993].

The 1971 M_W 6.7 San Fernando and 1994 M_W 6.7 Northridge earthquakes were an obvious target for imaging thrust ramps as, for instance, discussed by *Davis and Namson* [1994]. A thrust ramp model of these earthquakes would confine the deformation to the upper crust, which suggests that the high-velocity material should be confined below the regional detachment (Figure 13a). This type of structure was not observed in the 3-D V_P model (Figure 12). Instead, the high-V_P material is mostly located on the upthrown side of the fault planes as illustrated in Figure 13b, such as would occur when bringing lower crustal material up along more steeply dipping faults. Furthermore, in the case of the deeper Northridge earthquake, the high-V_P material appears to be within the lower crust.

The deformation of the hanging wall above thrust faults is best imaged around the edges of the basins. If the basins had continued to develop in transtensional environment, they would most likely have slopes dipping at about 45°

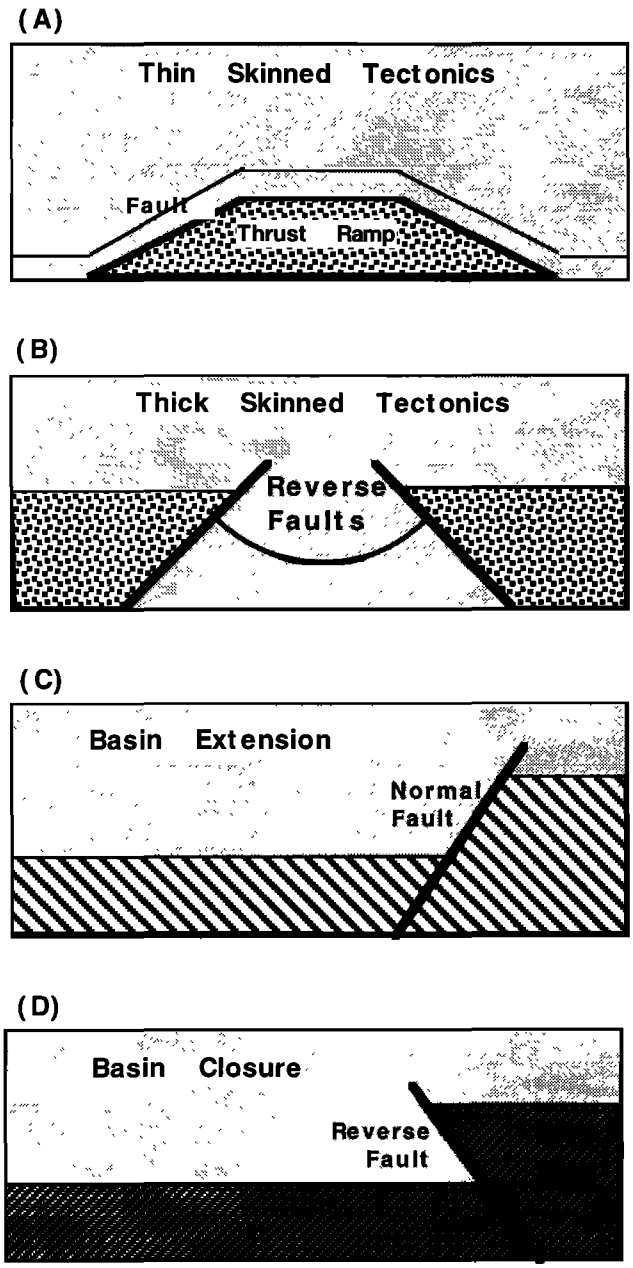

Figure 13. To illustrate the structural features such as basement and hanging wall deformation that we are looking for in the 3-D velocity model, we show schematic diagrams of (a) thin-skinned tectonics, (b) thick-skinned tectonics; (c) basin extension with normal faulting, and (d) basin closure with reverse faulting. These idealized models are not unique and are not required but would be supporting evidence for the existence of current tectonic deformation. The darker shading implies higher velocities at greater depth.

toward the center of the basin (Figure 13c). However, because the basins have been deformed by transpression and associated thrust faulting over the last 4 million years, we expect to find some evidence for vertical or overturned walls at the edges of the basins (Figure 13d). The south slopes of both the Ventura and the Los Angeles basin mostly reflect the original normal faulting with gently dipping slopes. In contrast, the sharp slopes on the north and northeast side, at 5 to 8 km depth in the Los Angeles basin and 8 to 12 km depth in the Ventura basin, dip steeply into or away from the center of the basins, suggesting apparent ongoing deformation of the hanging wall and closure of both basins (Figures 10, 11, and 12).

The 3-D velocity model thus suggests that the present crustal shortening in the region involves both the lower and upper crust. The lower crust appears to participate at least in part by up thrusting and possible delamination of the upper part of the lower crust into the upper crust. The upper crustal shortening causes basin closure and uplift of topography.

The hypocenters of the M>5.9 earthquakes mostly abut the high-velocity zones (see Figure 3, the 16 km depth section). If future moderate-sized or large earthquakes have similar geometrical relationship with these high-velocity zones, it is possible to speculate on their locations. Some regions that have similar velocity structure as the source region of the Northridge earthquake are (1) the region to the west of the Northridge rupture zone, (2) the V_P high beneath and to the south of the Verdugo Mountains, (3) the region south of the Whittier Narrows epicenter, and (4) the west end of the Palos Verdes Peninsula.

The shapes of the basins also affect the amplitude and duration of ground shaking [*Steidl et al.*, 1995; *Olsen et al.*, 1995]. Because the basins have steeply dipping walls on the north side, these may be more likely to reflect waves and cause amplification and extend the duration of the ground shaking. The sedimentary wedges to the south and west that dip into the basins will not reflect seismic waves efficiently but cause localized reverberations of constructive and destructive interference.

Conclusions

The Los Angeles and east Ventura basins extend to depths of 8 and 12 km. Their sedimentary fill have low V_P and in some instances high V_P/V_S as compared to the surrounding hard rock. The high V_P/V_S indicates the presence of near-surface water-saturated cracks. The crustal structure beneath the basins differs significantly. To the south, the Los Angeles basin is underlain by high-V_P rocks consistent with the north end of the Peninsular Ranges batholith, while the east Ventura basin is underlain by high-V_P and high-V_P/V_S mafic crust, possibly an ophiolitic sequence. The normal V_P and low V_P/V_S beneath Santa Monica Bay suggest the presence of a flake of quartz-rich continental crust.

The 3-D V_P model in some cases shows the sides of the basins steeply dipping away from the basin, thus providing some evidence for the closure of the basin, especially along their north side. Such basin shapes may be caused by deformation of the hanging wall, above thrust faults at depth. These steeper walls of the basins may extend the duration of long-period shaking within the basin.

At seismogenic depths of 16 km the hypocenters of moderate-sized and large earthquakes are located within or adjacent to high-V_P velocity bodies. In most cases these high-velocity bodies form the upper block, consistent with shortening of the lower crust as described in thick-skinned tectonic interpretations. This suggests that the shortening

of the lower crust is not occurring along ramps protruding from a regional subhorizontal decollement but rather involves delamination of material along thrust faults up into the upper crust. In turn, the upper crust shortens by closing the major basins and by creating topography.

Appendix: Details of Inversion Approach

Signals Being Modeled

The basic data used in the velocity inversion are the earthquake travel time residuals determined for each event-station pair located within the model area. The goal of the 3-D velocity inversion is to reduce the travel time residuals as much as possible by inverting for a 3-D velocity model with a realistic model length, which is defined here as the model standard deviation [*Evans et al.*, 1994]. One way to evaluate conceptually the performance of the inversion is to determine the average station residuals for each station at each grid spacing. If the gradational inversions are successful, all the residuals should decrease and approach zero as the grid spacing becomes denser.

The initial *P* and *S-P* station residuals were calculated with respect to the 1-D starting model with 40 km grid size

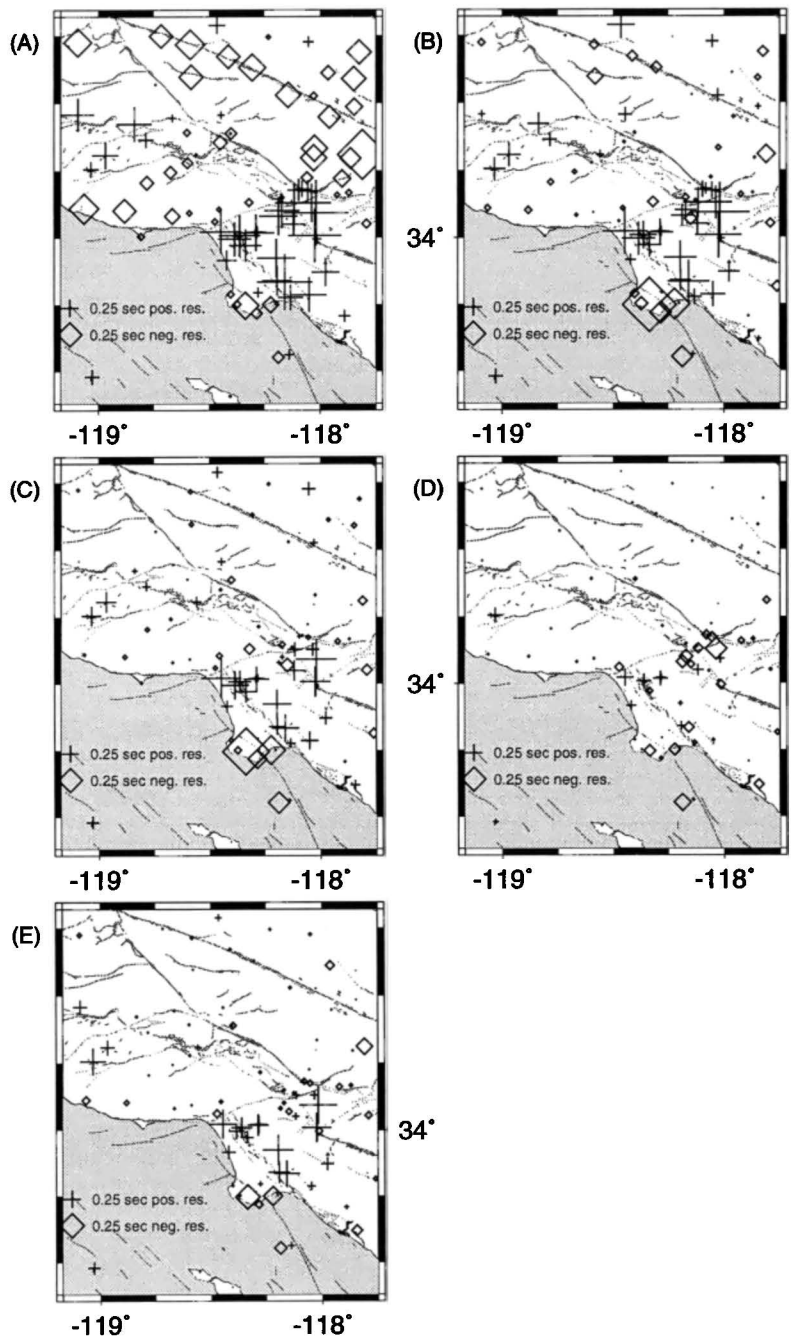

Figure A1. Station residuals for the *P* arrivals from the different inversions. (a) Initial residuals referenced to the 1-D starting model (LA0), (b) residuals relative to the 40 km grid 3-D model (LA1-40), (c) residuals relative to the 20 km grid 3-D model (LA1-20), (d) residuals relative to the 10 km grid 3-D model (LA1-10), and (e) the residuals relative to 10 km grid model determined from a uniform 10 km grid starting model (LA2-10).

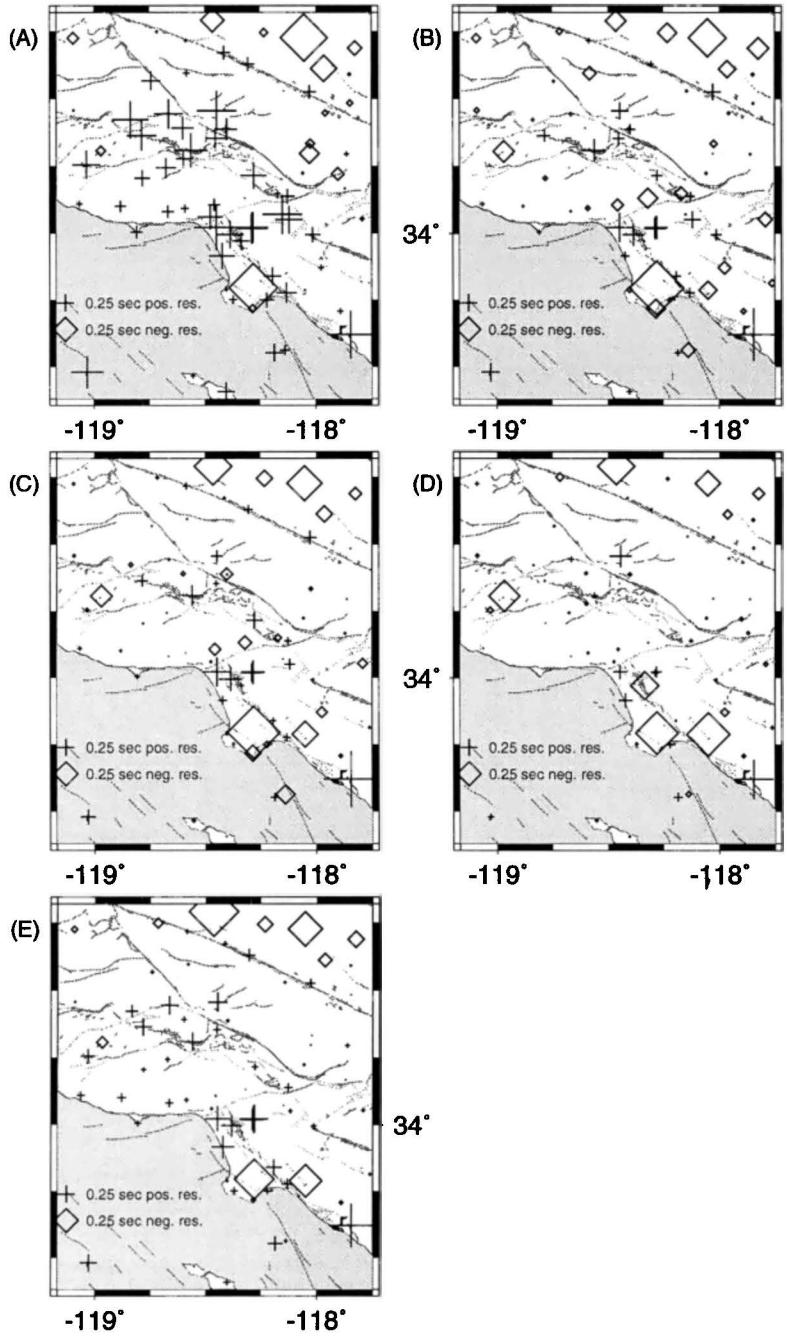

Figure A2. Station residuals for the *S-P* arrivals from the different inversions. (a) Initial residuals referenced to the 1-D starting model (LA0), (b) residuals relative to the 40 km grid 3-D model (LA1-40), (c) residuals relative to the 20 km grid 3-D model (LA1-20), (d) residuals relative to the 10 km grid 3-D model (LA1-10), and (e) the residuals relative to 10 km grid model determined from a uniform 10 km grid starting model (LA2-10).

(Figures A1 and A2). The positive residuals are observed at stations located on sediments in the basins and negative residuals at stations located at bedrock sites in the mountains. All of the residuals decrease as the 3-D models become more complex through successive iterations and finer grid spacing. The *P* residuals decrease significantly more than the *S-P* residuals, reflecting the higher quality of the *P* data.

The gradational inversion reduces the scatter in the travel time residuals and any possible distance bias in the distribution (Figure A3). The overall distribution that was contoured to show the details of the distribution consists of over 119,000 points for the V_P model and more than 16,000 points for the V_P/V_S model. In general, the distribution of residuals becomes narrower with decreasing grid space. The gradational models LA1-40 through LA1-10 result in an overall narrower distribution of residuals than the 10 km grid model (LA2-10) and provide a better representation of the overall velocity structure.

Model Damping

To ensure that the 3-D velocity model is as a realistic image of the true 3-D velocity structure as possible, the

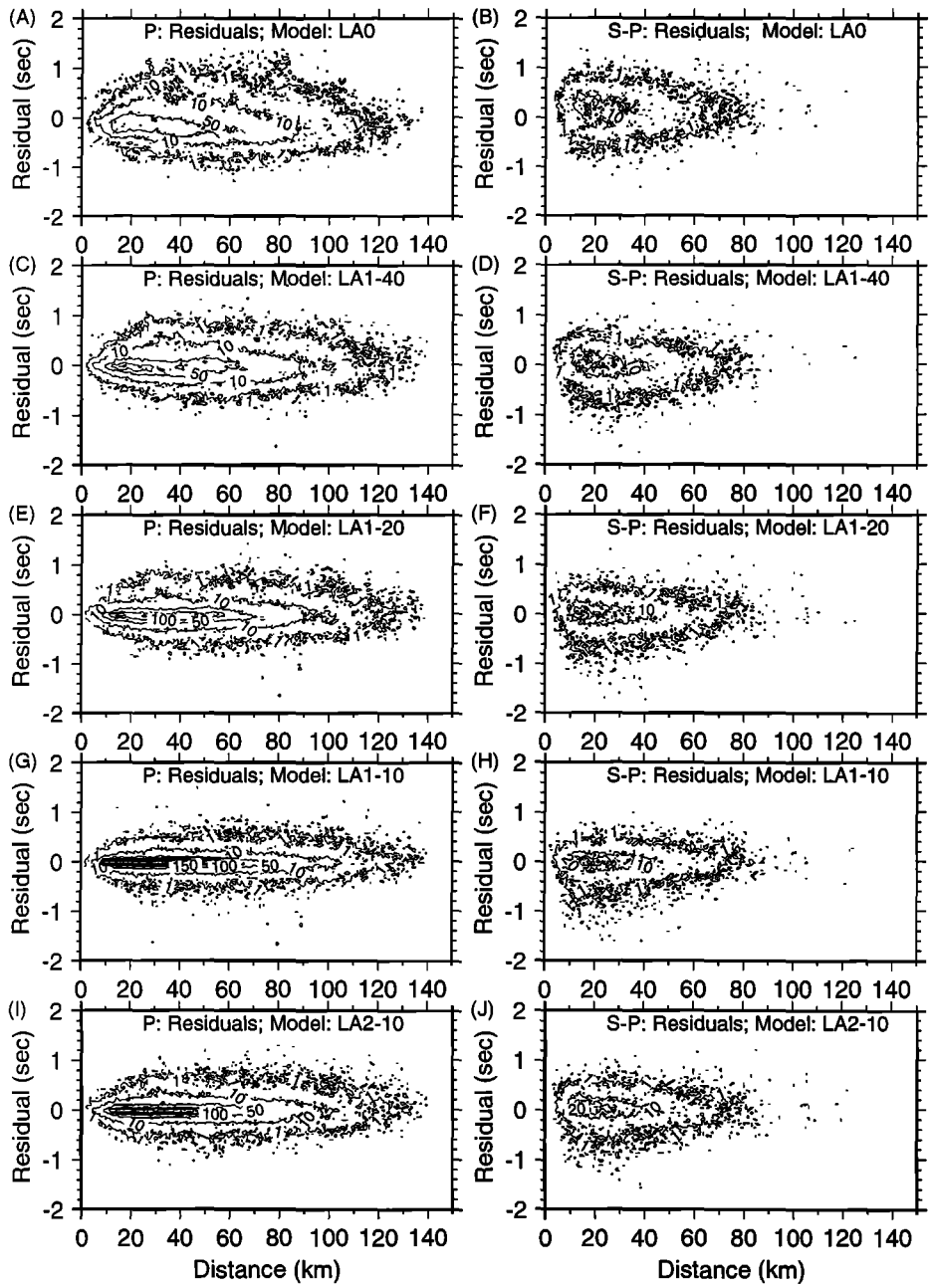

Figure A3. Residuals versus epicentral distance for both *P* and *S-P* data sets. (a and b) The initial *P* and *S-P* residuals referenced to the 1-D starting model; (c and d) residuals relative to the 40 km grid 3-D model; (e and f) residuals relative to the 20 km grid 3-D model; (g and h) delays relative to the 10 km grid 3-D model; (i and j) the residuals relative to 10 km grid model determined from a 10 km grid uniform starting model.

damping parameter has to be chosen carefully. The model length of the 3-D model will grow to an unreasonable size if too small a damping value is used.

The damping parameter balances the two factors that damped least squares minimizes [*Eberhart-Phillips,* 1993]:

$$\min(\sum r^2 + \varepsilon^2|\Delta m|^2) \qquad \text{(A1)}$$

The damping parameter ε is adjusted because all the residuals r can not be explained by perturbations to model parameters Δm and on succeeding iterations Σr^2 does not decreased at the same rate as $|\Delta m|^2$ toward zero. In real data, there will be a portion of the residuals that will be left even after the inversion has converged to an acceptable model. In our interactive inversion we adjusting the damping value after each iteration based both on the damping selected for the initial iterations and on the current residuals and model perturbations. We recompute the damping value so that the ration c remains constant over all iterations [*Eberhart-Phillips,* 1993]:

$$c = \frac{\varepsilon^2|\Delta m|^2}{\sum r^2} \qquad \text{(A2)}$$

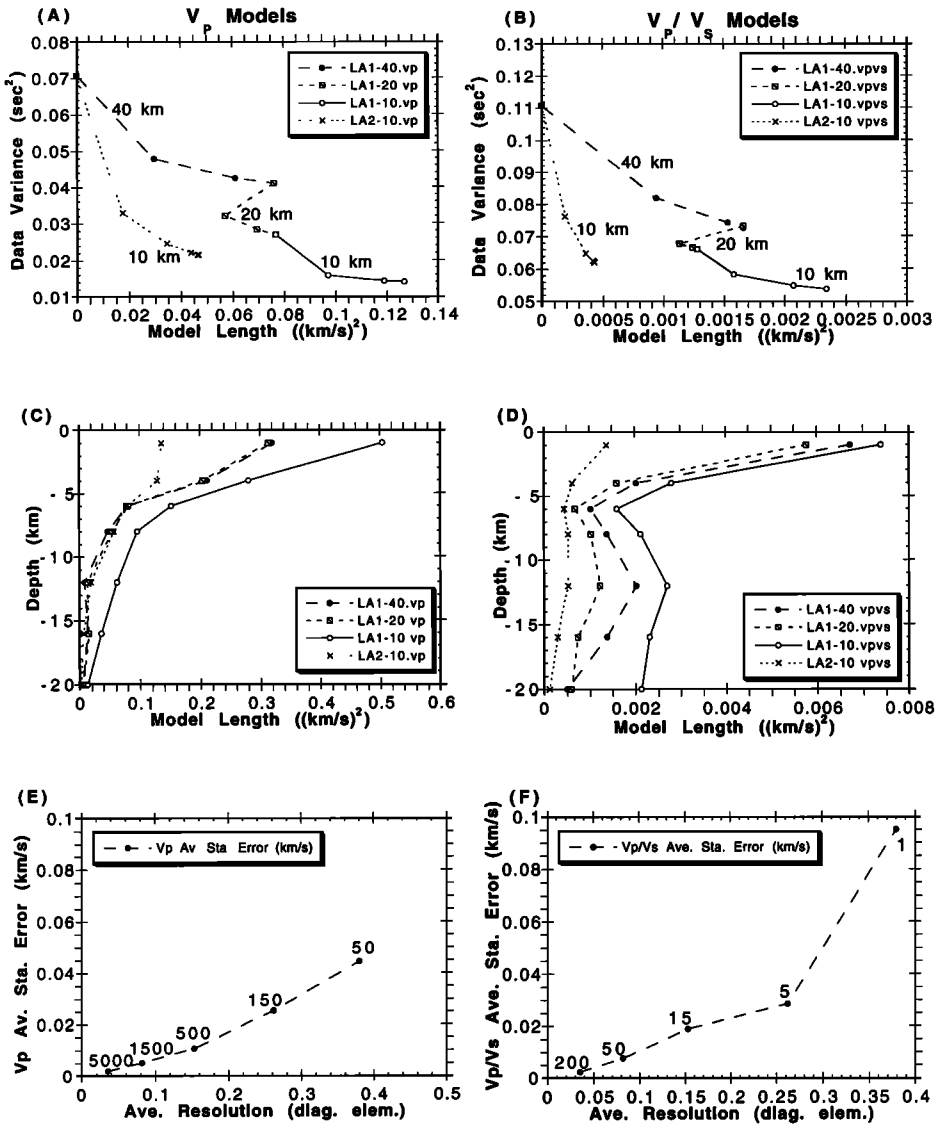

Figure A4. (a and b) Data variance versus model length for P and S-P data sets for gradational inversions with grid spacing of 40, 20, and 10 km. Also shown is the data variance for the 10 km grid model based on a 10 km grid uniform starting model. (c and d) The model length versus depth for the V_P and V_P/V_S models as above. (e and f) Average standard error versus average resolution diagonal elements for different damping values for the 10 km grid of the gradational 3-D inversion.

This method of selecting the damping causes it to increase with successive iterations.

The data variance decreases as a function of increasing model length with decreasing grid spacing, for a fixed value of the damping parameter (Figures A4a and A4b). The V_P model length is larger than the V_P/V_S model length in part because the V_P/V_S ratio is a small quantity that shows small spatial variations. For comparison, both the inversion from a plain uniform 10 km velocity grid and the gradational models are shown. More iterations from a uniform model do not significantly decrease the data variance but rather simply increase the model length at a high rate. The gradational models accomplish significantly more reduction in the data variance while approximately doubling the overall model length. The increase in mode length takes place mostly in the two top layers of the models (Figures A4c and A4d). This is consistent with the general observation that near-surface velocities can vary extremely rapidly over small distances, for instance, between soft, unconsolidated sediments and hard rock outcrops.

Several runs were performed for the 10 km grid of the gradational inversion to select the most reasonable final damping parameter for the damped least squares inversion [*Thurber*, 1983]. The smaller the damping, the higher the resolution and the larger the average standard error is (Figures A4e and A4f). We chose V_P damping of 150 and V_P/V_S damping of 15 as a trade-off between too high standard errors reasonable resolution.

In general, the damping for the V_P models is higher than for the V_P/V_S models simply because the P data set is bigger than the S-P data set. The S-P data are of inherently lower quality than the P data because some stations only have a

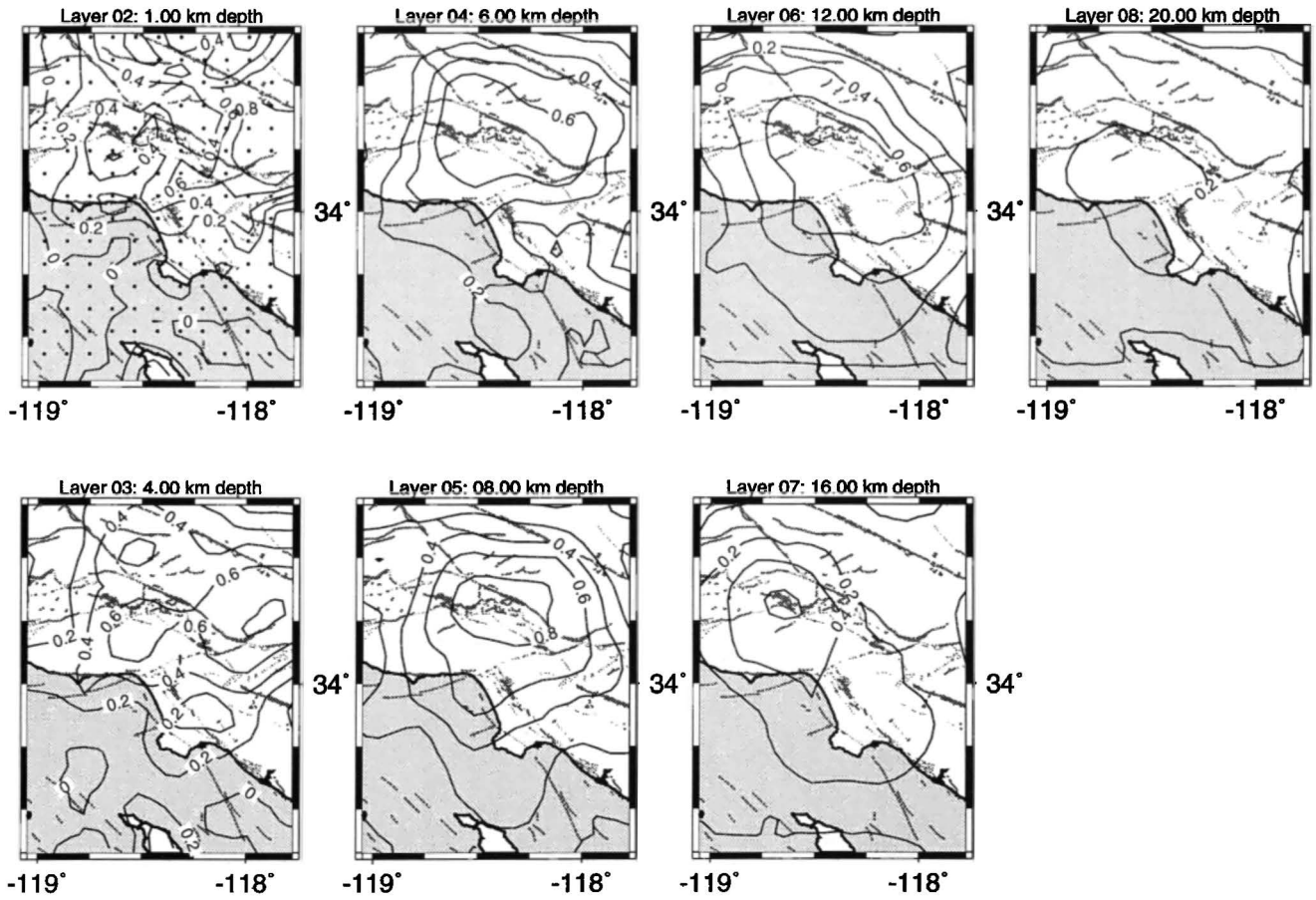

Figure A5. Diagonal elements of the resolution matrix for the final 10 km grid gradational V_P model (LA1-10) shown in seven depth slices at depths of 1, 4, 6, 8, 12, 16, and 20 km depth. The 1 km depth slice shows the velocity grid points.

vertical seismometer that may not allow an accurate estimate of the S arrivals. The V_P/V_S models thus need to be interpreted more carefully than the V_P models.

Model Quality

Errors in the final 3-D velocity models and the final 3-D locations result from nonlinearity, initial velocity model, parameterization, data errors, ray-tracing method, and uneven ray coverage. The nonlinearity, initial velocity model, and parameterization error were addressed by trying different grids, different iteration strategies such as gradational inversion, and different initial models. We have determined the resolution matrix and the corresponding resolving width function and standard error to evaluate the effects of data errors, ray-tracing method, and uneven ray coverage.

Resolution. The model resolution matrix R for the damped least squares problem that we solve is [*Menke*, 1989]

$$R = \left(M^T M + L\right)^{-1} M^T M \qquad \text{(A3)}$$

where M is a matrix of partial derivatives as described above. The model resolution is the identity matrix with perfect resolution, if the diagonal elements of the damping matrix L are all zero.

The central part of the model area shows high resolution (0.4 to 0.8), while the edges and the offshore area to the southwest show low resolution (0.2 or less) (Figure A5). The spatial velocity anomalies do not seem to be artifacts because there are no apparent correlations between regions of low resolution and the anomalies in the final models in Figures 3 and 4.

Standard error. We use the model standard error to provide an estimate of the mapping of the data error into the model error. The model standard error σ is related to the data error σ_d by [*Menke*, 1989]

$$\sigma^2 = (\sigma_d)^2 \mathrm{diag}(C) \qquad \text{(A4)}$$

where C is the covariance matrix

$$C = (M^T M + L)^{-1}\left[\left(M^T M + L\right)^{-1}\right]^T \qquad \text{(A5)}$$

The standard error determined from the covariance matrix varies throughout the model with errors ranging from 0.02 to 0.04 km/s (Figure A6). Other studies using

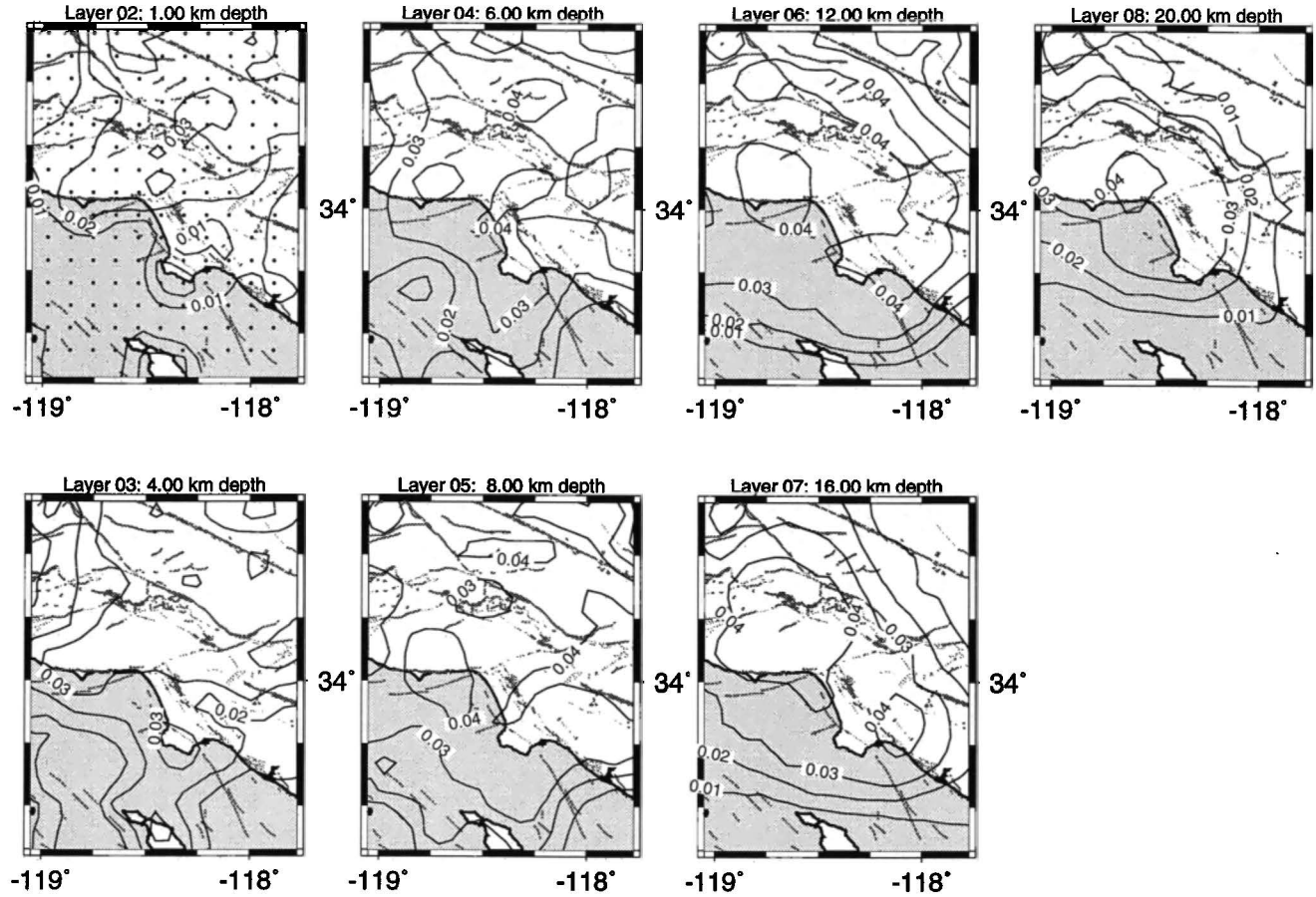

Figure A6. Standard error for the final 10 km grid gradational V_P model (LA1-10) shown in seven depth slices at depths of 1, 4, 6, 8, 12, 16, and 20 km depth. The 1 km depth slice shows the velocity grid points.

the same SIMULPS approach have shown that the calculated standard error should be multiplied by a factor of 2 [*Thurber*, 1983] to obtain realistic standard error estimates or a factor of 5 to obtain very conservative error estimates [*Foulger et al.*, 1995].

Derivative weighted sum. The model fidelity is discussed below in terms of the spread function and its relation to the derivative weighted sum (DWS). *Toomey and Foulger* [1989] define the DWS of the nth velocity parameter α_n as

$$DWS(\alpha_n) = N \sum_i \sum_j \left\{ \int_{Pij} \omega_n(x) ds \right\} \quad \text{(A6)}$$

where i and j are the indices for event and station, w is the linear interpolation weight and depends on coordinate position, P_{ij} is the ray path from i to j, and N provides normalization for the volume influenced by α_n [*Toomey and Foulger*, 1989].

The DWS is a better measure of information density provided by the ray coverage than counting the number of rays [*Toomey and Foulger*, 1989]. The DWS in this study is much larger than reported for other studies in part because most studies use data from about 300 to 500 earthquakes while this study uses data from 5225 earthquakes (Figure A7).

Spread function. To evaluate where the model parameters are well resolved, we determined both the full resolution matrix and the spread function of each averaging vector. We calculate the spread function from the resolution matrix following *Michelini* [1991] as

$$S_j = \log\left(|S_j|^{-1} \sum_{k=1}^{N} \left(\frac{S_{kj}}{|S_j|} \right)^2 D_{jk} \right) \quad \text{(A7)}$$

where S_{kj} are the elements of the resolution matrix R, and D_{jk} are the distances to adjacent nodes. The elements of the resolution matrix are normalized such that the sum of their squares is equal to 1. $|S_j|$ is the L_2 norm and is a weighting factor that accounts for the value of the resolution kernel for each parameter. A well-defined parameter has a small resolving width, while less well-defined parameters have broad kernel shapes and small overall values of the resolving kernel [*Michelini*, 1991].

An averaging vector is a row in the resolution matrix. Where the density of seismic rays is high within the model we expect good resolution and small values of the spread function [*Michelini*, 1991]. In some cases model parameters may be constrained, even though the diagonal elements of the resolution matrix are less than 0.4, provided

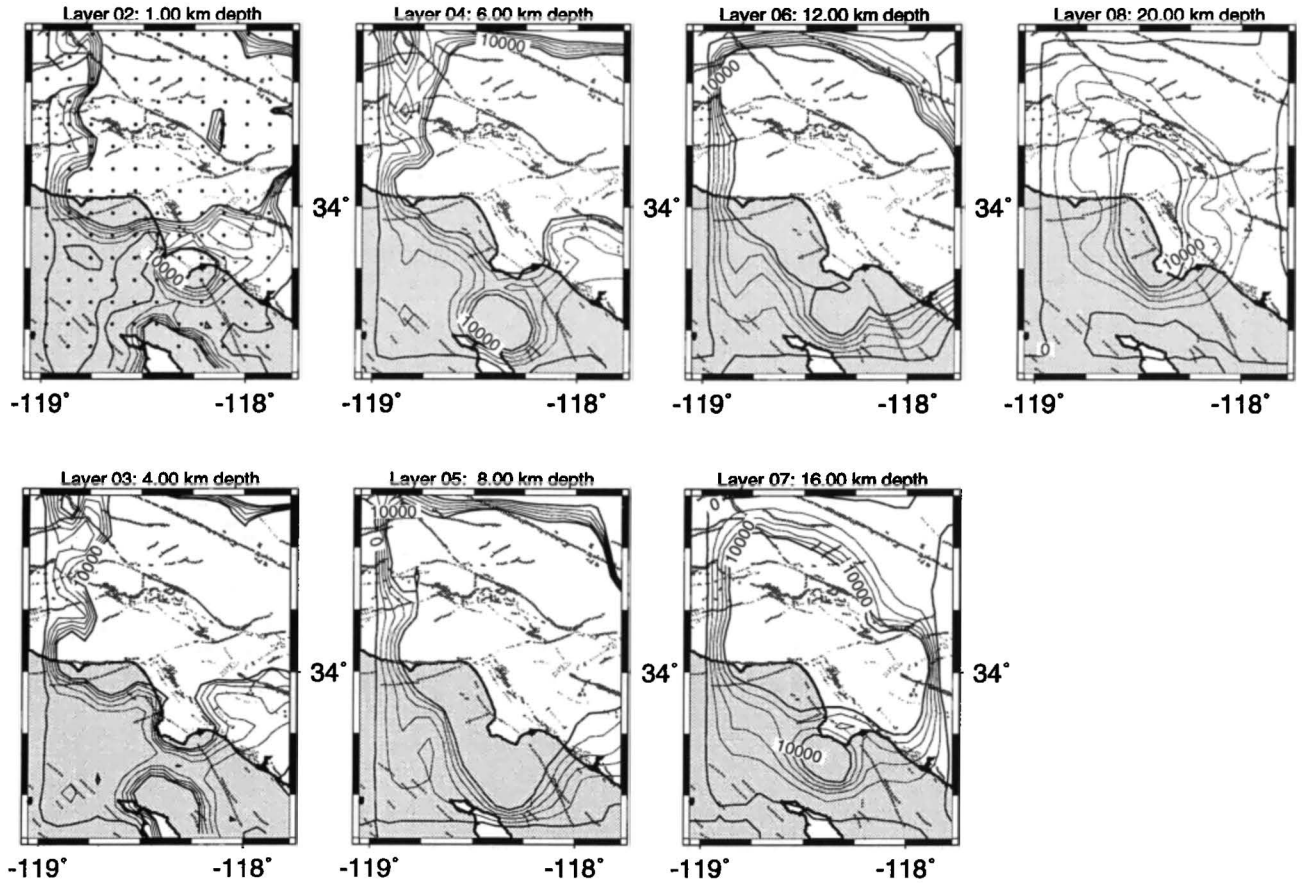

Figure A7. Derivative weighted sum for the final 10 km grid gradational V_P model (LA1-10) shown in seven depth slices at depths of 1, 4, 6, 8, 12, 16, and 20 km depth. The 1 km depth slice shows the velocity grid points.

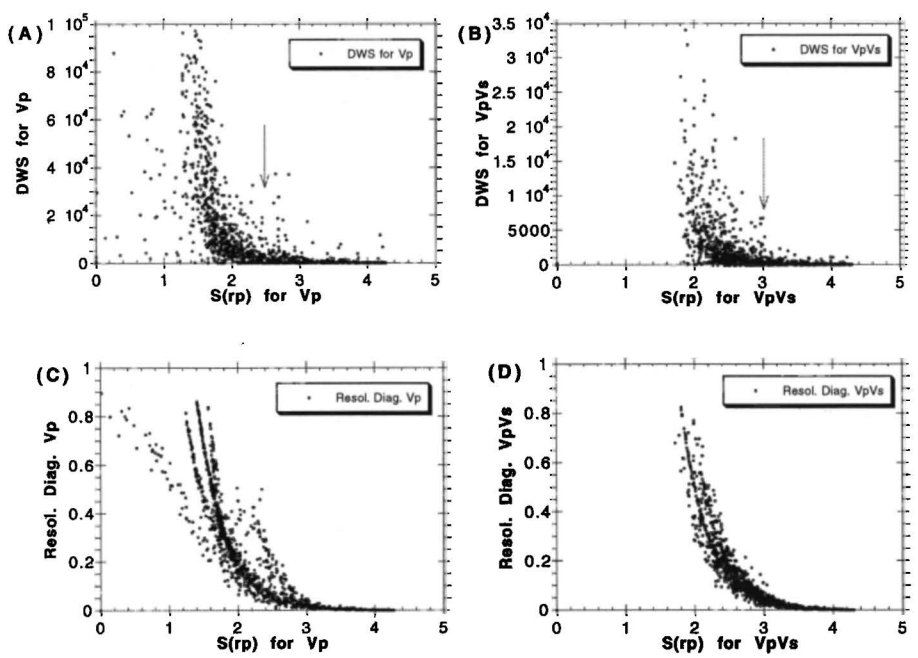

Figure A8. (a and b) derivative weighted sum (DWS) versus spread function values for V_P and V_P/V_S models (LA1-10). (c and d) Diagonal elements of the resolution matrix versus spread function values for the V_P and V_P/V_S models. The arrows show the selected value of the spread function for the V_P *and* V_P/V_S models plotted in subsequent figures.

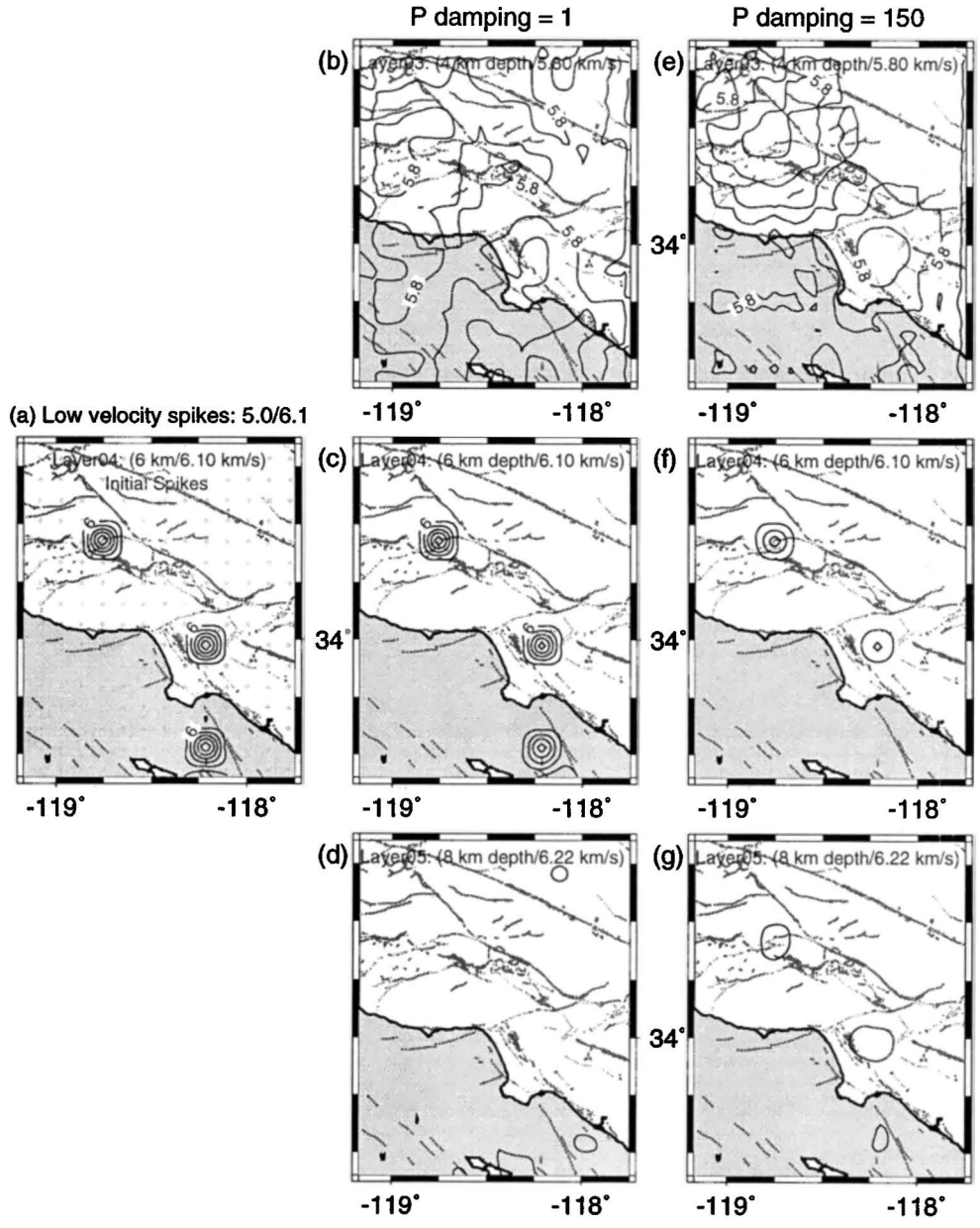

Figure A9. Spike tests using the V_P model. (a) Two low-velocity spikes are assigned to two grid nodes in the east Ventura and Los Angeles basins at depth of 6 km. (b, c, and d) Recovered spikes using damping of 1. (e, f, and g) Recovered spikes using damping of 150, same as was used in the final model.

the density of rays is sufficiently high to yield small values of the spread function [*Toomey and Foulger*, 1989].

The spread function can also be viewed as volume averaging around a grid node. The smaller the value of the spread function, the more compact the averaging vector is and the better the volume averaging is centered around the desired grid node. We plotted the contours of the spread function in Figures 3 and 4 to delineate areas of the model that are well resolved.

The derivative weighted sum (DWS) is an average relative measure of the density of rays near a grid node [*Toomey and Foulger*, 1989]. The DWS is sensitive to the spatial distance between a ray and a grid node and is better than an unweighted count of the total number of rays. To determine a suitable range for the spread function, we have plotted DWS versus the spread function values for the final model (Figure A8). We have also shown the diagonal elements of the resolution matrix as a function of the spread function value. The nodes with high density of rays have small spread function values and are well resolved. Both of these plots show that a spread function value of 2.5 or less for the V_P model and 3.0 or less for the V_P/V_S model delineate the well-determined regions of the models.

To evaluate the effectiveness of the spread function to determine, where the model is adequately well resolved, we also plotted the diagonal elements of the resolution matrix as a function of the spread function and corresponding DWS values (Figure A8). Both of these plots show the same behavior, allowing the spread function to delineate the well-resolved parts of the model.

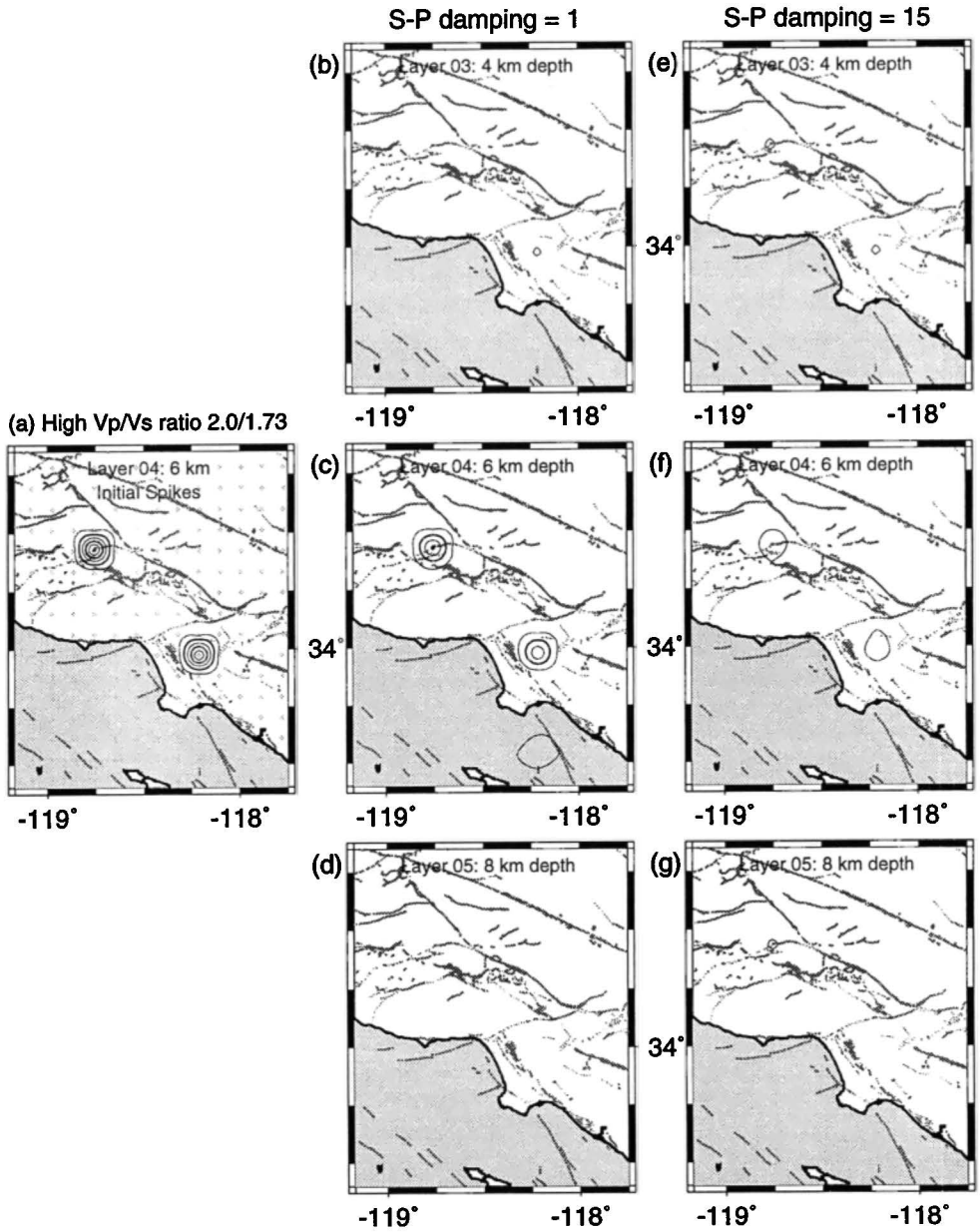

Figure A10. Spike tests using the V_P/V_S model. (a) Two low-velocity spikes are assigned to two grid nodes in the east Ventura and Los Angeles basins at depth of 6 km. (b, c, and d) Recovered spikes using damping of 1. (e, f, and g) Recovered spikes using damping of 15, same as was used in the final model.

In general, the resolution is acceptable or greater than 0.4 within the model region. The resolution ranges from 0.4 to 0.8 in the middle of the model and is smaller in the near-surface and the bottom layer at 20 km depth. The resolution is less than 0.3 offshore in the southwest part of the model. This region has few earthquakes and no stations except on the islands and thus the ray coverage is less dense than in other parts of the model.

Spike Tests

To test the results of the resolution matrix and the spread function calculations, we developed several spike models. The purpose of the spike models is to test how well anomalies are reproduced and if any artifacts are introduced, such as leaking of anomalies into adjacent nodes in three dimensions. We chose three nodes, east Ventura, Los Angeles, and San Pedro, in the 6 km layer to have velocity reduced from 6.1 to 5.0 km/s or 18% lower velocity (Figure A9). First, we calculated synthetic travel times using the original data set, and then, in turn, we invert from a 10 km grid model for the velocity structure. The P damping of 1 recreates all three spikes essentially indicating that without damping the SIMULPS code will recover the synthetic signal. A V_P damping of 150 that was used in the final models recovers about 54% and 32% of the anomalies in the two spikes in the Ventura and the Los Angeles basin. The spike test was repeated with 5% lower velocity, and the amplitude recovery was about 60% and 36%. In both cases the San Pedro channel spike was not

recovered, which is also consistent with the low resolution and high values of the spread function in this region.

The V_P/V_S spike model shows similar properties with 67% recovery of the anomaly for *S-P* damping of 1 and only 26% recovery of the anomaly for *S-P* damping of 15 (Figure A10). The spike models thus confirm that the data can recreate the synthetic anomalies, although the V_P data set does significantly better than the V_P/V_S data set.

Acknowledgments. S. Hough and L. Jones provided helpful critical reviews. G. Abers, T. Davis, and C. Jones provided constructive JGR reviews. We are grateful to the seismic analysts of Caltech, the USGS, and USC for competent processing of the earthquake data. We thank D. Eberhart-Phillips and C. Thurber for help with the SIMULFS code and R. Clayton, T. Wright, T. Brocher, and S. Chavez for constructive comments. This research was partially supported by USGS grant 1434-94-G-2440, USGS cooperative agreement 1434-95-A-01300, and NSF grant 94-16119 to Caltech. Southern California Earthquake Center publication 325; partial SCEC support from NSF Cooperative Agreement EAR-8920136 and USGS Cooperative Agreement 14-08-0001-A0899. Contribution 5672, Division of Geological and Planetary Sciences, California Institute of Technology, Pasadena. Electronic version of the velocity models is available form the first author via e-mail or from the Southern California Earthquake Center, Data Center, anonymous FTP at scec.gps.caltech.edu in /pub/hauksson.

References

Aki, K., Overview, in *Seismic Tomography; Theory and Practice*, edited by H. M. Iyer and K. Hirahara, pp. 1-8, Chapman and Hall, New York, 1993.

Bryant, A. S., and L. M. Jones, Anomalously deep crustal earthquakes in the Ventura basin, southern California, *J. Geophys. Res.*, *97*, 437-447, 1992.

Christensen, N. I., Poisson's ratio and crustal seismology, *J. Geophys. Res.*, *101*, 3139-3156, 1996.

Christensen, N. I., and W. D. Mooney, Seismic velocity structure and composition of the continental crust: A global view, *J. Geophys. Res.*, *100*, 9761-9788, 1995.

Crouch, J. K., and J. Suppe, Late Cenozoic tectonic evolution of the Los Angeles basin and inner California borderland: A model for core complex-like crustal extension, *Geol. Soc. Am. Bull.*, *105*, 1414-1434, 1993.

Crowell, J. C., Late Cenozoic basins of onshore southern California: Complexity is the hallmark of their tectonic history, in *Cenozoic Basin Development of Coastal California*, vol. 6, edited by R. V. Ingersoll and W. G. Ernst, pp. 207-241, Chapman and Hall, New York, 1987.

Davis, T. L., and J. S. Namson, A balanced cross-section of the 1994 Northridge earthquake, southern California, *Nature*, *372*, 167-169, 1994.

Davis, T. L., J. S. Namson, and S. Gordon, Structure and hydrocarbon exploration in the transpressive basins of southern California, in *Field Conference Guide 1996*, Pacific Section A.A.P.G., GB 73, edited by P. L. Abbott and J. D. Cooper, pp. 189-238, 1996.

Donnellan, A., B. H. Hager, R. W. King, and T. A. Herring, Geodetic measurement of deformation in the Ventura Basin region, southern California, *J. Geophys. Res.*, *98*, 21,727-21,739, 1993.

Eberhart-Phillips, D., Local earthquake tomography: earthquake source regions, in *Seismic Tomography: Theory and practice*, edited by H.M. Iyer and K. Hirahara, pp. 613-643, Chapman and Hall, New York, 1993.

Eberhart-Phillips, D., Three-dimensional *P* and *S* velocity structure in the Coalinga region, California, *J. Geophys. Res.*, *95*, 15,343-15,363, 1990.

Eberhart-Phillips, D., and A. J. Michael, Three-dimensional velocity structure, seismicity, and fault structure in the Parkfield region, central California, *J. Geophys. Res.*, *98*, 15,737-15,758, 1993.

Edelman, A., et al., Portable instrument data set from the January 17, 1994 Northridge earthquake aftershock sequence (abstract), *Eos Trans.(AGU)*, *75*, (44), Fall Meet. Suppl., F457, 1994.

Ehlig, P. L., Origin and tectonic history of the basement terrane of the San Gabriel Mountains, Central Transverse Ranges, in *The Geotectonic Development of California*, edited by W. G. Ernst, pp. 253-283, Berlin, Prentice-Hall, Inc., Englewood Cliffs, NJ, 1981.

Evans, J. R., D. Eberhart-Phillips, and C. H. Thurber, User's manual for *SIMULPS12* for imaging V_p and V_P/V_S: A derivative of the "Thurber" tomographic inversion *SIMUL3* for local earthquakes and explosions, *U.S. Geol. Surv. Open File Rep.*, *94-431*, 1994.

Foulger, G. R., A. D. Miller, B. R. Julian, and J. R. Evans, Three-dimensional v_p and v_p/v_s structure of the Hengill Triple Junction and geothermal area, Iceland, and the repeatability of tomographic inversion, *Geophys. Res. Lett.*, *22*, 1309-1312, 1995.

Fuis, G. S., et al. , Images of crust beneath southern California will aid study of earthquakes and their effects, *Eos, Trans. AGU, 77,* 173,176, 1996.

Given, D. D., and C. L. Koesterer, Station arrival data for a quarry blast on Santa Catalina Island, California, *U.S. Geol. Surv., Open File Rep,. 83-462*, 12, 1983.

Haase, J. S., E. Hauksson, F. Vernon, and A. Edelman, Modeling of ground motion from a 1994 Northridge aftershock using a tomographic velocity model of the Los Angeles Basin, *Bull. Seismol. Soc. Am.*, *86*, S156-S167, 1996.

Hadley, D., and H. Kanamori, Seismic structure of the Transverse Ranges, California, *Geol. Soc. Am. Bull.*, *88*, 1469-1478, 1977.

Hafner, K., and R. W. Clayton, Crustal Structure Beneath the San Gabriel Mountains, CA. (LARSE), (abstract) *Eos, Trans. AGU, 76,* (46), Fall Meet. Suppl, F348, 1995.

Hauksson, E., Earthquakes, faulting, and stress in the Los Angeles Basin, *J. Geophys. Res.*, *95*, 15,365-15,394, 1990.

Hauksson, E., and G. V. Saldivar, Seismicity and active compressional tectonics in Santa Monica Bay, southern California, *J. Geophys. Res.*, *94*, 9591-9606, 1989.

Hauksson, E., T.-L. Teng, and T. L. Henyey, Results from a 1500 m deep, three-level downhole seismometer array: Site response, low Q values and $f_{\max}$, *Bull. Seismol. Soc. Am.*, *77*, 1883-1904, 1987.

Hauksson, E., L. M. Jones, and K. Hutton, The 1994 Northridge earthquake sequence in California: Seismological and tectonic aspects, *J. Geophys. Res.*, *100*, 12,335-12,355, 1995.

Hearn, T. M., and R. W. Clayton, Lateral velocity variations in southern California I. Results for the upper crust from P_g waves, *Bull. Seismol. Soc. Am.*, *76*, 495-510, 1986.

Hu, G., W. Menke, and C. Powell, Polarization tomography for *P* wave velocity structure in southern California, *J. Geophys. Res.*, *99*, 15,245-15,256, 1994.

Huftile, G., and R.S. Yeats, Deformation rates across the Placerita (Northridge M_W = 6.7 aftershock zone) and Hopper Canyon segments of the western transverse ranges deformation felt, *Bull. Seismol. Soc. Am., 86,* S3-S18, 1996.

Jennings, C. W., Fault map of California with volcanoes, thermal springs and thermal wells, scale1:750,000, Geol. Data Map 1 ed. Calif. Div. of Mines and Geol., Sacramento, 1975.

Kissling, E., W. L. Ellsworth, D. Eberhart-Phillips, and U.

Kradolfer, Initial reference models in local earthquake tomography, *J. Geophys. Res.*, *99*, 19,635-19,646, 1994.
Langston, C., Scattering of teleseismic body waves under Pasadena, California, *J. Geophys. Res.*, *94*, 1935-1951, 1989.
Lutter, W. J., C. Thurber, and G. S. Fuis, An image of the upper 5 km from inversion of first arrivals from the 1994 LARSE Experiment: Line 1 from Seal Beach to El Mirage Lake (abstract), *Eos, Trans., AGU, 76*, (46), Fall Meet. Suppl., F348, 1995.
Luyendyk, B. P., M. J. Kamerling, and R. Terres, Geometric model for Neogene crustal rotations in southern California, *Geol. Soc. of Am. Bull.*, *91*, 211-217, 1980.
Magistrale, H., and H.-W. Zhou, Lithologic control of the depth of earthquakes in southern California, *Science*, *273*, 639-642, 1996.
Magistrale, H., H. Kanamori, and C. Jones, Forward and inverse three-dimensional *P* wave velocity models of the southern California crust, *J. Geophys. Res.*, *97*, 14,115-14,135, 1992.
Magistrale, H., K. McLaughlin, and S. Day, A geology-based 3D velocity model of the Los Angeles Basin sediments, *Bull. Seismol. Soc. Am.*, *86*, 1161-1166, 1996.
Menke, W., *Geophysical Data Analysis: Discrete Inverse Theory*, pp. 1-289, Academic, San Diego, Calif., , 1989.
Michelini, A., Fault zone structure determined through the analysis of earthquake arrival times, Ph.D. thesis, 191 pp., Univ. of Calif., Berkeley, 1991.
Mori, J., D. J. Wald, and R. L. Wesson, Overlapping fault planes of the 1971 San Fernando and 1994 Northridge, California, earthquake, *Geophys. Res. Lett.*, *22*, 1003-1036, 1995.
Nicholson, C., and D. W. Simpson, Changes in V_p/V_s with depth: Implications for appropriate velocity models, improved earthquake locations, and material properties of the upper crust, *Bull. Seismol. Soc. Am.*, *75*, 1105-1123, 1985.
Norris, J. J., and R. W. Clayton, Analysis of the offshore-onshore data collected during the 1994 LARSE survey (abstract), *Eos Trans. AGU*, *76*,(46), Fall Meet. Suppl., F348, 1995.
Olsen, K. B., R. J. Archuleta, and J. R. Matarese, Three-dimensional simulation of a magnitude 7.75 earthquake on the San Andreas Fault, *Science*, *270*, 1628-1632, 1995.
Pavlis, G. L., and J. R. Booker, The mixed discrete-continuous inverse problem: Application to the simultaneous determination of earthquake hypocenters and velocity structure, *J. Geophys. Res.*, *85*, 4801-4810, 1980.
Perkins, G., Data report for the 1987 seismic calibration/refraction survey, Whittier, California, 29 pp., U.S. Geol. Surv., Menlo Park, Calif., 1988.
Real, C. R., Seismicity and tectonics of the Santa Monica-Hollywood-Raymond Hill fault zone and northern Los Angeles basin, Los Angeles County, California, Transverse Ranges, *U.S. Geol. Surv. Prof. Pap. 1339.*, 113-124, 1977.
Scholz, C., *The Mechanics of Earthquakes and Faulting*, pp. 1-439, Cambridge Univ. Press , New York, 1989.
Silver, L. T., Some observations on the basement rocks along the LARSE line (abstract), *Eos Trans., AGU, 76*, (46), Fall Meet. Suppl., F347, 1995.
Sorensen, S., Petrologic evidence for Jurassic, island-arc-like basement rocks in the southwestern Transverse Ranges and California Continental Borderland, *Geol. Soc. Am. Bull.*, *96*, 997-1005, 1985.
Steidl, J. H., L. F. Bonilla, and A. G. Tumarkin, Site effect study in the San Fernando Basin, Los Angeles, California: A comparison of methods (abstract), *Eos, Trans., AGU, 76*, (46), Fall Meet. Suppl., F351, 1995.
Sung, L., and D. D. Jackson, Crustal and uppermost mantle structure under southern California, *Bull. Seismol. Soc. Am.*, *82*, 934-961, 1992.
Thurber, C. H., Earthquake locations and three-dimensional crustal structure in the Coyote Lake area, central California, *J. Geophys. Res.*, *88*, 8226-8236, 1983.
Thurber, C. H., Local earthquake tomography: Velocities and V_p/V_s—Theory, in *Seismic Tomography: Theory and Practice*, edited by H. M. Iyer and K. Hirahara, pp. 563-583, Chapman and Hall, New York, 1993.
Thurber, C. H., and S. R. Atre, Three-Dimensional V_p/V_s variations along the Loma Prieta rupture zone, *Bull. Seismol. Soc. Am.*, *83*, 717-736, 1993.
Toomey, D. R., and G. R. Foulger, Tomographic inversion of local earthquake data from the Hengill-Grensdalur central volcano complex, Iceland, *J. Geophys. Res.*, *94*, 17,497-17,510, 1989.
Um, J., and C. H. Thurber, A fast algorithm for two-point seismic ray tracing, *Bull. Seismol. Soc. Am.*, *77*, 972-986, 1987.
Wessel, P., and W. H. F. Smith, Free software helps map and display data, *Eos Trans. AGU*, *72*, (41), 441,445-446, 1991.
Wright, T. L., Structural geology and tectonic evolution of the Los Angeles basin, California, *AAPG Mem.*, *52*, 35-134, 1991.
Yeats, R. S., Converging more slowly, *Nature*, *366*, 299-301, 1993.
Yeats, R. S., and G. J. Huftile, The Oak Ridge fault system and the 1994 Northridge earthquake, *Nature*, *373*, 418-420, 1995.
Yeats, R. S., G. J. Huftile, and L. T. Stitt, Late Cenozoic tectonics of the East Ventura Basin, Transverse Ranges, California, *AAPG Bull.*, *78*, 1040-1074, 1994.
Yerkes, R. F., T. H. McCulloh, J. E. Schoellhamer, and J. G. Vedder, Geology of the Los Angeles basin, California—An introduction, *U.S. Geol. Surv. Prof. Pap.*, *420-A*, A1-A57, 1965.
Zhao, D., and H. Kanamori, The 1994 Northridge earthquake: 3-D crustal structure in the rupture zone and its relation to the aftershock locations and mechanisms, *Geophys. Res. Lett.*, *22*, 763-766, 1995.

J. S. Haase and E. Hauksson, Seismological Laboratory, 252-21, Division of Geological and Planetary Sciences, 1200 E. California Blvd., California Institute of Technology, Pasadena, CA 91125. (e-mail: hauksson@gps.caltech.edu)

(Received April 10, 1996; revised October 7, 1996; accepted October 16, 1996).